

بص

RESEARCH ARTICLE

10.1029/2024SW003958

Key Points:

- OSSE study assessing hypothetical radio occultation (RO) constellations, the first to comprehensively account for forecast model and Abel inversion errors
- The RO constellation with low- and high-inclination orbits at 520 km altitude performs the best with the highest observation counts
- Uncharacterized Abel inversion errors and poorly retrieved low plasma density limit assimilation impact on the equatorial ionosphere

Supporting Information:

Supporting Information may be found in the online version of this article.

Correspondence to:

N. Dietrich, Nicholas.Dietrich@colorado.edu

Citation:

Dietrich, N., Matsuo, T., Lin, C.-Y., diLorenzo, B., Lin, C. C.-H., & Fang, T.-W. (2024). Evaluating radio occultation (RO) constellation designs using observing system simulation experiments (OSSEs) for ionospheric specification. *Space Weather*, 22, e2024SW003958. https://doi.org/10.1029/2024SW003958

Received 15 APR 2024 Accepted 31 JUL 2024

Author Contributions:

Conceptualization: Nicholas Dietrich, Tomoko Matsuo, Charles Chien-Hung Lin Data curation: Nicholas Dietrich, Chi-Yen Lin, Brandon diLorenzo, Tzu-Wei Fang

Formal analysis: Nicholas Dietrich Funding acquisition: Tomoko Matsuo Investigation: Nicholas Dietrich, Tomoko Matsuo. Chi-Yen Lin

© 2024 The Author(s). This article has been contributed to by U.S. Government employees and their work is in the public domain in the USA.

This is an open access article under the terms of the Creative Commons
Attribution-NonCommercial-NoDerivs
License, which permits use and distribution in any medium, provided the original work is properly cited, the use is non-commercial and no modifications or adaptations are made.

Evaluating Radio Occultation (RO) Constellation Designs Using Observing System Simulation Experiments (OSSEs) for Ionospheric Specification

Nicholas Dietrich¹, Tomoko Matsuo¹, Chi-Yen Lin², Brandon diLorenzo¹, Charles Chien-Hung Lin³, and Tzu-Wei Fang⁴

¹Ann and H.J. Smead Aerospace Engineering Sciences, University of Colorado Boulder, Boulder, CO, USA, ²Center for Astronautical Physics and Engineering, National Central University, Taoyuan, Taiwan, ³Department of Earth Sciences, National Cheng Kung University, Tainan, Taiwan, ⁴Space Weather Prediction Center, National Oceanic and Atmospheric Administration, Boulder, CO, USA

Abstract Low Earth orbit (LEO) radio occultationlradio occultations (RO) constellations can provide global electron density profiles (EDPs) to better specify and forecast the ionosphere-thermosphere (I-T) system. To inform future RO constellation design, this study uses comprehensive Observing System Simulation Experiments (OSSEs) to assess the ionospheric specification impact of assimilating synthetic EDPs into a coupled I-T model. These OSSEs use 10 different sets of RO constellation configurations containing 6 or 12 LEO satellites with base orbit parameter combinations of 520 or 800 km altitude, and 24° or 72° inclination. The OSSEs are performed using the Ensemble Adjustment Kalman Filter implemented in the data assimilation (DA) Research Testbed and the Thermosphere-Ionosphere-Electrodynamics General Circulation Model (TIEGCM). A different I-T model is used for the nature run, the Whole Atmosphere Model-Ionosphere Plasmasphere Electrodynamics (WAM-IPE), to simulate the period of interest is the St. Patrick's Day storm on March 13–18, 2015. Errors from models and EDP retrieval are realistically accounted for in this study through distinct I-T models and by retrieving synthetic EDPs through an extension Abel inversion algorithm. OSSE assessment, using multiple metrics, finds that greater EDP spatial coverage leading to improved specification at altitudes 300 km and above, with the 520 km altitude constellations performing best due to yielding the highest observation counts. A potential performance limit is suggested with two 6-satellite constellations. Lastly, close examination of Abel inversion error impacts highlights major EDP limitations at altitudes below 200 km and dayside equatorial regions with large horizontal gradients and low electron density magnitudes.

Plain Language Summary The upper atmosphere, the region above 100 km altitude, is strongly influenced by space weather events that can negatively impact ground and space-based technologies. These technologies include communication and navigation systems impacted by radio wave propagation through high altitudes plasma, a region called the ionosphere. Developing observing systems that provide global monitoring of the ionosphere is a critical need for understanding and forecasting space weather changes, such as radio occultations (RO) that provide plasma observations using global positioning radio signals. In this study, we evaluate these hypothetical RO observing systems in simulated experiments using data assimilation (DA), an approach that integrates synthetic observations into a physics-based model. We find that increased observational coverage corresponds to better estimated plasma states, and that lower orbit altitude constellations yield higher observation counts. This study comprehensively incorporates model and observation errors to more realistically represent real-world conditions. One limitation of RO data is highlighted in regions near the equator and at lower altitudes (below 250 km) where there is a breakdown in assumptions for observation retrieval. This study illustrates the clear operational benefits of these plasma observations, informing the future observing system design and aiding their use for space weather forecasting.

1. Introduction

Monitoring the near-Earth space environmental conditions for space weather now-casting and forecasting is increasingly pertinent to maintaining critical ground- and space-based technological systems. One such critical impact is ionospheric plasma disturbances affecting navigational systems via the propagation of radio waves for Global Navigation Satellite Systems (GNSS) and very low frequency signals, along with other communication systems utilizing high frequency and ultra high frequency radio signals. The peak heights and magnitudes of

DIETRICH ET AL. 1 of 20



10.1029/2024SW003958

Methodology: Nicholas Dietrich, Chi-

Yen Lin

Project administration: Tomoko Matsuo **Resources:** Tomoko Matsuo

Software: Nicholas Dietrich, Chi-Yen Lin

Supervision: Nicholas Dietrich,

Tomoko Matsuo

Validation: Nicholas Dietrich

Visualization: Nicholas Dietrich,

Brandon diLorenzo

Writing - original draft:

Nicholas Dietrich

Writing – review & editing:

Tomoko Matsuo, Chi-Yen Lin, Charles Chien-Hung Lin plasma density affects whether radio signals are reflected or absorbed, the index of refraction that bends these signals, and small-scale plasma density irregularities can cause radio signals to scatter or scintillate. These space weather effects on radio signals can be characterized using parameters, such as the F-region peak electron density, N_mF_2 , and its height, h_mF_2 , the total electron content (TEC), the rate of change of TEC index (ROTI), and the S_4 index. Geomagnetic storms can induce considerable variations and disturbances of the near-Earth plasma environments, stressing our radio-based systems as indicated by dramatic changes in ROTI and S_4 index (e.g., Moreno et al., 2011). As underscored by the Promoting Research and Observations of Space Weather to Improve the Forecasting of Tomorrow (PROSWIFT) Act in 2020 (Lugaz, 2020) and space weather gap analysis findings (Vourlidas et al., 2023), continuing and developing new ionospheric observing systems, as well as their integration into forecast models with the help of data assimilation (DA), is essential for advancing space weather now-casting and forecasting capabilities. Moreover, the Weather Research and Innovation Forecasting Act of 2017 specifically mandates the National Oceanic and Atmospheric Association (NOAA) to perform Observing System Simulation Experiments (OSSEs), wherein DA frameworks are used to quantitatively assess hypothetical observing systems for their relative value and benefit.

GNSS constellations are designed for global positioning, enabling radio occultation (RO) observations with global coverage of the ionosphere. Currently available GNSS constellations include GPS, GLONASS, Galileo, and BeiDou. The development and operation of RO satellite constellations have considerably grown over recent decades, providing real-time observations for ionospheric space weather prediction, climatological study, and insight into ionospheric physics. In addition to their well-recognized and valuable role as an observing system for ionospheric plasma density, recent DA studies (Dietrich et al., 2022; Matsuo & Hsu, 2021) suggest their utility as a global monitoring system of thermospheric mass density. Earth-based RO constellations began in 1995 with the launch of MicroLab-1 Global Positioning System/Meteorology (GPS/MET) (Hajj & Romans, 1998; Kursinski et al., 1997), and was succeeded in 2006 by the FORMOSAT-3/COSMIC (F3/C) (Anthes et al., 2008) and its follow-on mission FORMOSAT-7/COSMIC-2 (F7/C2) (Fong et al., 2019; Yue, Schreiner, Pedatella, et al., 2014) in 2019. F3/C consisted of a 6-satellite low Earth orbit (LEO) constellation, orbiting in separate orbital planes, each at 72° latitude and 800 km altitude. RO observations counts of F3/C were doubled with the launch of the more recent F7/C2, a 6-satellite constellation in a similar orbit configuration at 24° inclination and 550 km altitude. Commercial RO sources have additionally grown to include satellites and constellations in near polar orbit (e.g., Angling et al., 2021), promoting their use within DA experiments quantifying their benefit, that is, RO Modeling EXperiment (ROMEX) (Anthes et al., 2023).

RO soundings have provided a wealth of ionospheric information to produce 3-dimensional, global observations of the ionosphere. During an RO sounding, the slant TEC is measured along the radio signal's limb sounding geometry connecting the GNSS satellite and the observing LEO satellite. Electron density profiles (EDPs) are consequently retrieved from these slant TEC observations at the ray tangent point locations through Abel inversion, with this inversion relying on a spherical symmetry assumption. RO EDPs are highly accurate observations of the ionosphere's F-region, generally around 300–400 km altitude, especially for F_2 region parameters N_mF_2 and h_mF_2 (Cherniak et al., 2021; Lei et al., 2007; Yue et al., 2010). Relatively large errors can exist for low altitudes, that is, the E-region below 200 km altitude (Kelley et al., 2009). Large RO EDP errors are also reported where there are breakdowns in the spherical symmetry assumption such as near equatorial latitudes (Tsai et al., 2001; Tsai & Tsai, 2004) and beneath the crests of the equatorial ionization anomaly (EIA), peaking at 200% (Liu et al., 2010; Yue et al., 2010). Recent algorithm improvements have been made to the Abel inversion retrieval, aided by prior ionosphere information (e.g., Chou et al., 2017; Lin et al., 2020; Pedatella et al., 2015; Tulasi Ram et al., 2016; Yue et al., 2013), or using a bottom-up retrieval for the D- and E-regions (Wu, 2018).

OSSEs have been used to quantitatively evaluate the value of RO observations (e.g., Forsythe et al., 2021; He et al., 2019; Hsu et al., 2018; Lee et al., 2013; Lin et al., 2015, 2017; Pedatella et al., 2020; Scherliess et al., 2004; Yue, Schreiner, Kuo, et al., 2014). Within an OSSE, synthetic data are generated from a nature run model simulation (that serves as a truth model) and then assimilated into a biased forecast model to assess improvement. Yue, Schreiner, Kuo, et al. (2014) performed an OSSE study prior to the launch of F7/C2, assessing the multiple planned RO EDPs from F7/C2 using NeQuick model as the nature run and assimilating EDPs into the empirical ionospheric model IRI. Lee et al. (2013) assimilated synthetic F7/C2 EDPs into a coupled ionosphere-thermosphere (I-T) physics-based model, and saw global improvements in electron density states over previous F3/C EDPs. Further to realistically assess the value of observing systems, it is crucial to quantify observation errors for DA. In particular, RO EDP assimilation can be negatively impacted by Abel retrieval errors if not

DIETRICH ET AL. 2 of 20

15427390, 2024, 8, Downloaded from https://agupubs.onlinelibrary.wiley.com/doi/10.1029/2024SW003958 by University

Figure 1. The OSSE framework used in this study, separated by blocks for the nature run, retrieval of synthetic observations, DART-TIEGCM cycling and post-analysis. Data are represented by parallelograms and arrows indicate workflow direction.

properly characterized, with most recent RO error quantification performed in Yue et al. (2010), Liu et al. (2010). Even though OSSEs have been proven to be useful for mission planning and in informing the most effective constellations designs, previous OSSE work has yet to account for both forecast model errors and Abel retrieval errors in a comprehensive manner. For example, the tropospheric weather forecasting community has been investing considerable efforts to design standard and fair nature runs for OSSE studies (e.g., Andersson & Masutani, 2010; Errico et al., 2013; Hoffman & Atlas, 2016; Masutani et al., 2007). These standardized nature runs use state-of-the-art numerical model simulations that climatologically match the real atmosphere and contain realistic differences from the forecast model.

This study aims to evaluate the value of different RO constellation designs by quantifying the ionospheric specification impact of assimilating EDP observations into a coupled I-T model. We do this by adopting a comprehensive OSSE approach that overcomes the limitations of past RO EDP OSSE studies. The nature run is performed using the Whole Atmosphere Model-Ionosphere Plasmasphere Electrodynamics (WAM-IPE) (Akmaev, 2011; Maruyama et al., 2016), and the forecast coupled I-T model used in the DA framework is the Thermosphere Ionosphere Electrodynamics General Circulation Model (TIEGCM) developed by the National Center for Atmospheric Research (NCAR) (Qian et al., 2014; Richmond et al., 1992). Here, synthetic EDPs are retrieved from the WAM-IPE nature run simulation through an extensive Abel inversion procedure combined with simulated RO limb sounding geometries between the GNSS and hypothetical RO constellations. This Abel inversion procedure is built on the operational procedure used for the COSMIC-2 EDP data product. Synthetic EDP observations used in this study therefore include realistic Abel inversion errors, that cannot be represented by directly sampling electron density from the nature run at RO tangent points. We run a widely-used ensemble DA framework developed by NCAR's Data Assimilation Research Testbed (DART) (Anderson et al., 2009) with TIEGCM, denoted as DART-TIEGCM. The Ensemble Adjustment Kalman Filter (EAKF) is used (Anderson, 2001). The OSSEs are run for a popularly studied event, the week of the March 2015 St. Patrick's day storm. A total of 10 OSSEs are performed for the different permutations of the four base virtual LEO constellation configurations. To address what constellation design is "best," evaluated across different ionospheric regions, the results from these OSSEs are compared using various metrics including key ionospheric parameters of TEC, N_mF_2 and h_mF_2 , as well as the three-dimensional plasma density structure.

In the following sections, Section 2 provides details for the EDP Abel retrieval and its errors as well as the OSSE design. Section 3 provides the OSSE results, including assimilation impact, a relative OSSE ranking metric and a potential limit to observation impact. Section 4 contains general discussion assessing observation impact from DART-TIEGCM and Abel inversion errors, along with future work. Finally, Section 5 provides the conclusions.

2. Methods

A general overview of the OSSE framework is shown in Figure 1 with four workflow blocks: nature run, synthetic RO observations, DART-TIEGCM and post-analysis. In the nature run block, a single model run instance is used to represent the "true" atmosphere, here using the WAM-IPE model that is detailed in Section 2.2. In the synthetic RO observation block, the assimilated observations are retrieved from the nature run output through simulating RO events between the RO and GNSS constellations. Each OSSE has an associated set of retrieved EDP

DIETRICH ET AL. 3 of 20

observations as well as corresponding observation uncertainty quantification that is detailed in Section 2.3. The DART-TIEGCM block contains the DA cycle where synthetic observations and the TIEGCM experiment model are combined together and are discussed in Section 2.1. More details of how the TIEGCM ensembles are initialized and other experiment information are included in Section 2.4. The remaining block is the post-analysis in which the estimated TIEGCM states (posteriors) are directly compared against the WAM-IPE nature run, discussed in Section 3.

2.1. Data Assimilation: DART-TIEGCM

In this study, we employ an ensemble-based approach, specifically the EAKF as developed and implemented by DART (Anderson, 2001; Anderson et al., 2009). In ensemble DA, states and their uncertainties are represented with ensembles in an Monte Carlo approach tailored for high-dimensional state estimation. The typical cycle of the EAKF consists of two steps: (a) The forecast step that propagates model states with the full non-linear model dynamics and (b) the analysis step that optimally updates states using observation information. The forecast step produces a forecast, or prior state, that is used in the analysis step to produce an analysis estimate, or posterior. The DA cycle continues, feeding the posterior into the next forecast step. In the EAKF, each observation has a spatially localised impact on model states determined by ensemble covariance information. This covariance information determines the statistical relationship between an observation and nearby surrounding model states, and is dynamically estimated from model ensembles that reflect nonlinear dynamics and physics. Further information for how DART-TIEGCM can be used is found in other studies (e.g., Chartier et al., 2016; Chen et al., 2016; Dietrich et al., 2022; Hsu et al., 2014; Kodikara et al., 2021; Lee et al., 2012; Matsuo et al., 2013). The DART software is detailed in Anderson et al. (2009), Anderson and Collins (2007) with additional DART tutorial information available in the Open Research Section.

We use the TIEGCM v2.0 developed by NCAR as the forecast model, solving a self-consistent solution of first-principle equations of the I-T system and producing the three-dimensional, time-varying field of the thermosphere and ionosphere states. The 5° resolution version of TIEGCM is used, with 29 pressure levels with half scale-height resolution that spans from ~97 to ~500 km altitudes, depending on the solar conditions. External forcing in TIEGCM is specified through solar ultraviolet irradiance parameterized with respect to a daily value of the F10.7 index (F10.7), and lower boundary tides through the Global Scale Wave Model (GSWM). The magnetospheric forcing is specified by the empirical Heelis convection model and an empirical auroral model.

2.2. Nature Run (Truth) Model: WAM-IPE

The nature run simulation, which serves as the truth model, is achieved with a free-run of the I-T coupled physics-based model WAM-IPE developed by NOAA. There are a number of differences in how the I-T physics and dynamics are solved between TIEGCM and WAM-IPE. It is expected that these differences manifest as forecast model biases and likely widen during the storm-period. WAM is a spectral whole atmosphere model, containing 150 pressures levels that solves neutral states from the surface up to 400–600 km altitudes, output at about 2° horizontal resolution (Akmaev, 2011). IPE solves plasma state physics along flux tubes in the semi-Lagrangian reference frame, extending up into the plasmasphere encompassing 90 to 10,000 km altitudes (Maruyama et al., 2016). In contrast, TIEGCM solves both neutral and plasma states in the Euler reference frame, approximating the O⁺ flux at the upper boundary, and using lower boundary tide conditions specified by GSWM. In WAM-IPE, solar irradiance is also parameterized using daily F10.7 but magnetospheric forcing is specified by an empirical Weimer convection model driven by solar wind states at 1-min cadence. These model differences are expected to introduce distinctive ionosphere biases partly corrected by assimilation of EDP observations. The details for the WAM-IPE nature run and TIEGCM experiment ensembles are available in Section 2.4, and the Open Research Section.

2.3. Virtual Constellations

For this study, we use four base virtual LEO constellation configurations, derived from the F3/C and F7/C2 constellations, to design 10 different sets of hypothetical RO constellation configurations. Each base constellation consists of six satellites with the same inclination and altitude and at separate orbital planes. We simulate RO events between GPS and GLONASS and LEO satellite constellations in a similar mode of operation used by F7/C2. The base constellation parameters are as follows: (a) A 520 km altitude and 24° inclination constellation

DIETRICH ET AL. 4 of 20

 Table 1

 List of 10 OSSEs for Different Base Low Earth Orbit Satellite Constellation Designs

Experiment name	LEO constellations	Short-hand notation
OSSE 1	520 km alt, 24° inc	5024
OSSE 2	520 km alt, 72° inc	5072
OSSE 3	800 km alt, 24° inc	8024
OSSE 4	800 km alt, 72° inc	8072
OSSE 5	520 km alt, 24° inc and 800 km alt, 72° inc	5024 and 8072
OSSE 6	520 km alt, 24° inc and 520 km alt, 72° inc	5024 and 5072
OSSE 7	520 km alt, 24° inc and 800 km alt, 24° inc	5024 and 8024
OSSE 8	$800 \text{ km alt, } 24^{\circ} \text{ inc and } 800 \text{ km alt, } 72^{\circ} \text{ inc}$	8024 and 8072
OSSE 9	520 km alt, 72° inc and 800 km alt, 72° inc	5072 and 8072
OSSE 10	520 km alt, 72° inc and 800 km alt, 24° inc	5072 and 8024

Note. For short-hand notation, the first two digits reference the constellation altitude and the last two digits reference the constellation inclination.

(similar to F7/C2), (b) a $520 \, \mathrm{km}$ altitude and 72° inclination constellation, (c) a $800 \, \mathrm{km}$ altitude and 24° inclination constellation, and (d) a $800 \, \mathrm{km}$ altitude and 72° inclination constellation (similar to F3/C). All 10 OSSE combinations of one or two base virtual constellations are detailed in Table 1. Each OSSE is referenced according to a short-hand notation, with the first two digits referencing the constellation altitude, and the second two digits referencing the constellation inclination. For instance, OSSE 1, with the short-hand notation 5024, is performed using the LEO constellation of satellites at $520 \, \mathrm{km}$ altitude and 24° inclination.

Within each OSSE, we assimilate EDPs from 160 to 500 km altitude at 10 km vertical sampling intervals to update the DART state vector containing electron density, e^- , and atomic oxygen ion, O^+ . Gaussian uncorrelated noises are assigned to each electron density using the variances determined from the EDP uncertainty quantification process detailed in Section 2.3.2. The RO tangent point locations for each of these base constellations for a full day of observations is shown in Figure 2 to illustrate their respective coverage. As expected, the low-

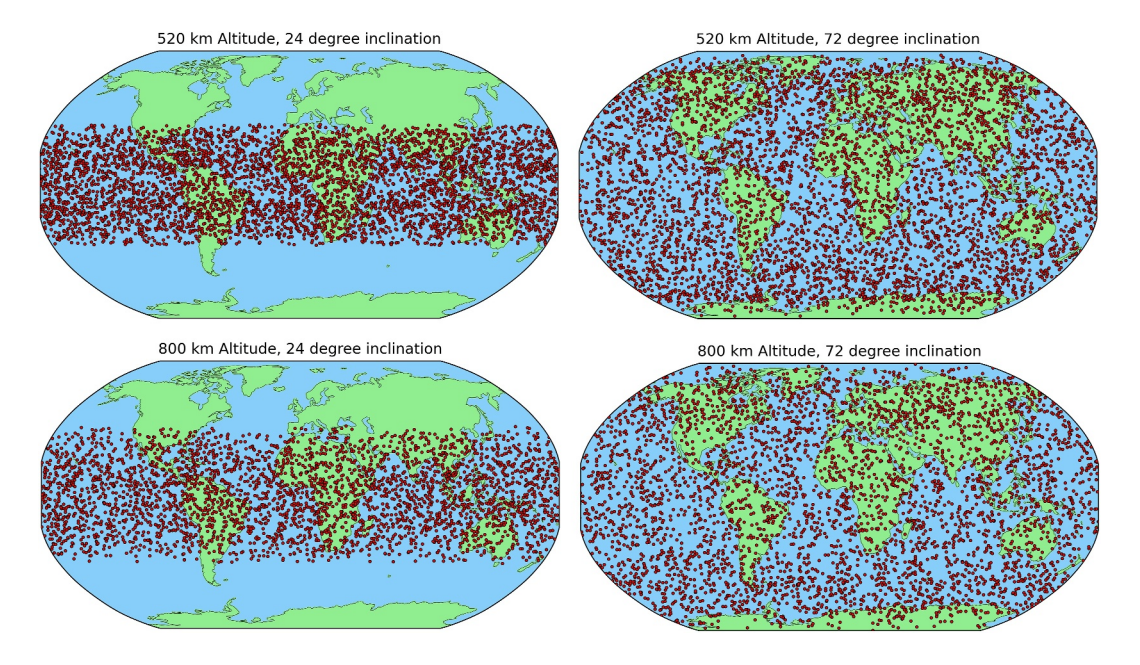


Figure 2. The radio occultation observation tangent points shown for the full day of March 13th at 300 km altitude. Shown for the four base virtual Low Earth orbit constellation configurations.

DIETRICH ET AL. 5 of 20



10.1029/2024SW003958

inclination constellations provide only low- and mid-latitude observations, while the high-inclination constellations provide observations in all latitude regions, at the cost of less dense spatial coverage.

2.3.1. Synthetic EDP Retrieval Using RO Simulation and Abel Inversion

Synthetic RO EDPs are generated from the WAM-IPE nature run simulation with the typical EDP retrieval processes, as detailed in Hajj and Romans (1998), Schreiner et al. (1999). Specifically, we use the Abel inversion algorithm adapted from the operational data product procedure used to generate ionPrf files for F3/C and F7/C2. The sounding paths from GNSS satellites to LEO RO satellites are used to generate the synthetic slant TEC profiles. For a typical RO sounding there is an occultation side and an auxiliary side, where the auxiliary side passes through both the upper ionosphere and plasmasphere and the occultation side passes through the ionosphere, atmosphere and plasmasphere. Here, WAM-IPE's ionosphere extension provides plasmasphere information. The resulting calibrated slant TEC profile comes from subtracting the auxiliary side TEC profile from the occultation side TEC profile and contains only the impact of the ionosphere. The synthetic EDPs are then retrieved by applying Abel inversion to these synthetic calibrated slant TEC profiles. The synthetic EDP data retrieved in this study thus contain the same systemic error as real ionPrf data products, ensuring the OSSE results more closely reflect reality.

2.3.2. Uncertainty Quantification of Synthetic EDPs

To determine observation uncertainties necessary for DA, the EDP errors due to Abel inversion are quantified. Observation errors are calculated using the difference between synthetic EDPs and the modeled electron density distribution from the WAM-IPE nature run. Sample standard deviations are computed after binning difference data with respect to the following parameters: day of year, constellation inclination, altitude, magnetic latitude, and solar local time. Four solar local time (LT) bins are used: LTs 4-10, LTs 10-16, LTs 16-22, and LTs 22-4. LEO constellation altitude was found to have a negligible effect on errors. Similar studies with EDP observations have used percentage errors over local time, altitude, and magnetic latitude (Lee et al., 2013; Liu et al., 2010; Yue et al., 2010), while we quantify errors using standard deviation. Standard deviations are computed from EDP samples within ± 5 km for a given altitude, and within $\pm 5^{\circ}$ for a given latitude. An example of the calculated EDP uncertainties for March 13th at 300 km is shown in Figure 3. Notable features is the distinct difference in the error magnitude for the four solar local time bins and the impact that constellation inclination has on error magnitudes for the LT 16-22 in the equatorial latitudes. Over these local times, there are highly variable spatial features such as the EIA and the prereversal enhancement. The pronounced dependence on constellation inclinations can also be due to smaller low-latitude observation counts for the high inclination orbit (shown in Figure S1 in Supporting Information S1).

The Abel retrieval errors are furthermore characterized for N_mF_2 , h_mF_2 and over multiple EDP altitudes as shown in Figure 4. For N_mF_2 , we see peak errors of 85% near the south Atlantic anomaly (SAA), while the global error average is 18%, with structures following Earth's magnetic field lines. As expected, we see very small errors for h_mF_2 with percentage errors peaking at 17% and averaging 4%. As for altitude variations of errors, we see substantial errors at 200 km altitude, where these errors are considerably higher than previous studies that showed low altitude errors to peak around 200% (Liu et al., 2010; Yue et al., 2010). In these two studies, Liu et al. (2010) uses IRI as the truth model and Yue et al. (2010) uses NeQuick as the truth model, two very different models from WAM-IPE. These large errors are captured in the calculated observation uncertainties, and the DA impact is discussed later in Section 3. Errors are smaller at 300 km, with peaks along the magnetic and near the SAA. Outside these two regions, errors are below 40%, with a median error of 25%. For 400 and 500 km altitudes, we see increasingly smaller errors, with a peak error near the SAA and a global average of 17%. There are some spurious high errors seen at high latitudes where there are low observation counts. It is noted these errors are highly dependent on solar LT, with two example local time cases shown in Figures S2 and S3 in Supporting Information S1.

These large errors seen in Figure 4 come primarily from break-downs of the spherical symmetry assumption used in Abel inversion. The break-downs of this assimilation are expected to impact regions with large horizontal gradients in electron density distribution, such as near and below the magnetic equator and EIA. The impact is less acute with increasing altitude. These errors are well-captured within uncertainty calculations considered in this

DIETRICH ET AL. 6 of 20

15427390, 2024, 8, Downloaded from https://agupubs.onlinelibrary.wiley.com/doi/10.1029/2024SW003958 by University Of Colorado Boulder, Wiley Online Library on [21/06/2025]. See the Terms

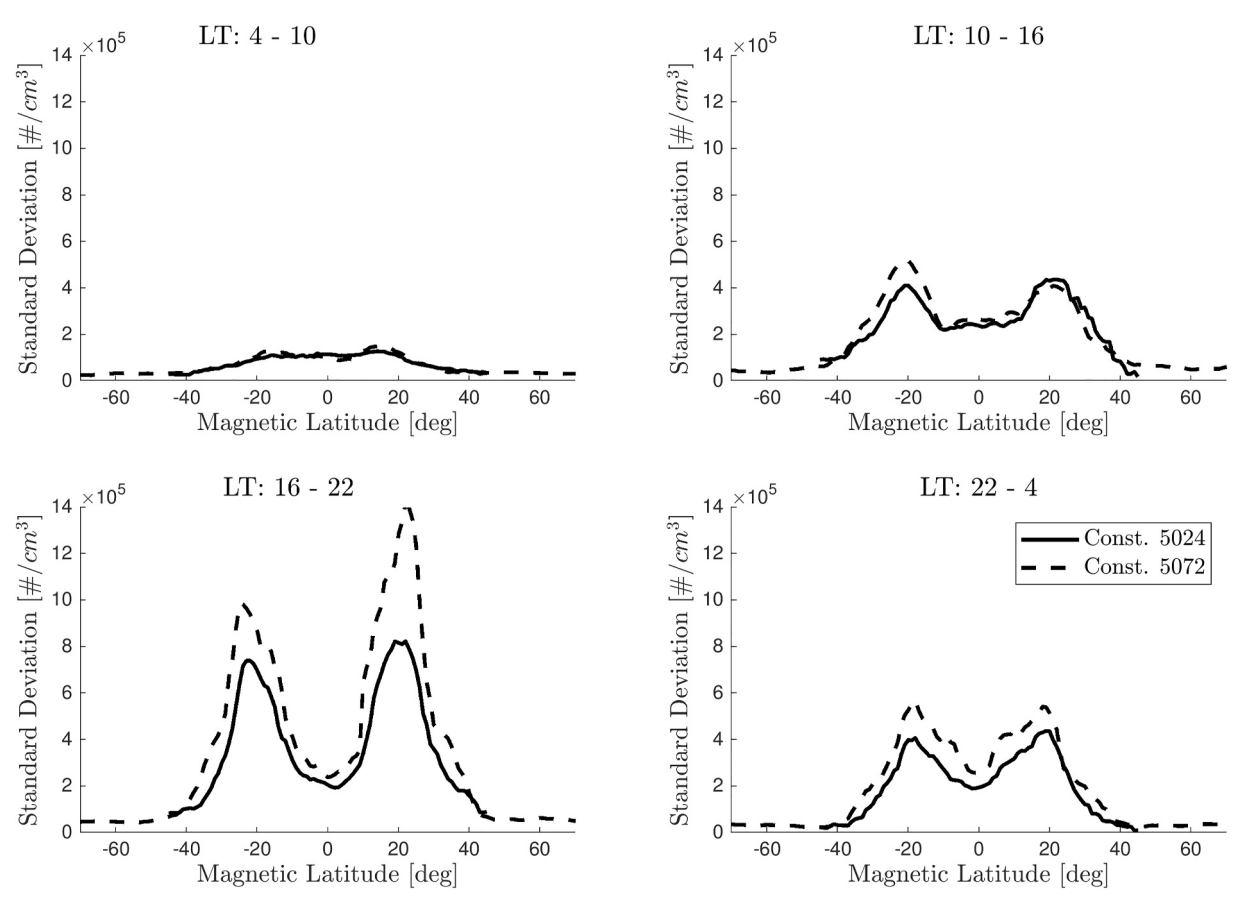


Figure 3. Standard deviations attributed to electron density profile (EDP) observations. Shown for two constellations, 5024 and 5072, at 300 km altitude on March 13th. Standard deviations are computed from the difference between synthetic EDPs and plasma density from the WAM-IPE nature run simulation after binning data with respect to day of year, constellation inclination, altitude, magnetic latitude, and solar local time.

study. An additional source of RO errors are from on-board GNSS receivers as well as receiver errors, but these errors are not considered in this study.

2.4. Experiment Set-Up

The OSSE period is the St. Patrick's day storm of March 2015, with observed solar and geomagnetic indices and interplanetary magnetic field (IMF) solar wind parameters are shown for this period in Figure 5. The nature run of WAM-IPE is a model free-run, specifying geomagnetic forcing using the Weimer model with input IMF solar wind parameters and the F10.7 index for solar irradiance. The OSSE is broken into two periods, the preceding quiet period and storm-time. The quiet period begins at UT00 on March 13th and ends at UT23 on March 16th. Localization is done using the Gaspari-Cohn (GC) function (Gaspari & Cohn, 1999) with a GC radius of 0.2 radians (\sim 1,300 km) without vertical localization, so observations have impact on all pressure levels. We do not use ensemble inflation. As the upper atmosphere is strongly influenced by external forcing, the TIEGCM ensemble is initialized using perturbed solar irradiance with the F10.7 index and geomagnetic indices driven with the Heelis model for 90 ensemble members. These perturbations are normally distributed and kept constant through the quiet period. The sampled F10.7 indices are sampled from $d_{F10.7} \sim \mathcal{N}(120,4^2)$ and Heelis input is defined through the hemispheric power, $d_{HP} \sim \mathcal{N}(22,4^2)$ and the cross-tail potential $d_{\Phi} \sim \mathcal{N}(46,8^2)$. Ensembles are initialized through a 7-day spin-up period to reach a steady-state for the start of the OSSE. For the storm period, TIEGCM magnetospheric drivers have updated samples, sampling from $d_{HP} \sim \mathcal{N}(115,10^2)$ and $d_{\Phi} \sim \mathcal{N}(135,20^2)$ with the same quiet period F10.7 samples.

Additional quality control is necessary for DA with observation flags and rejection to avoid assimilating poor quality observations. We reject observations for three reasons: negative values, outside an outlier threshold, and a

DIETRICH ET AL. 7 of 20

15427390, 2024, 8, Downloaded from https://agupubs.onlinelibrary.wiley.com/doi/10.1029/2024SW003958 by University Of Colorado Boulder, Wiley Online Library on [21/06/2025]. See the Terms and Conditions (https://onlinelibrary.

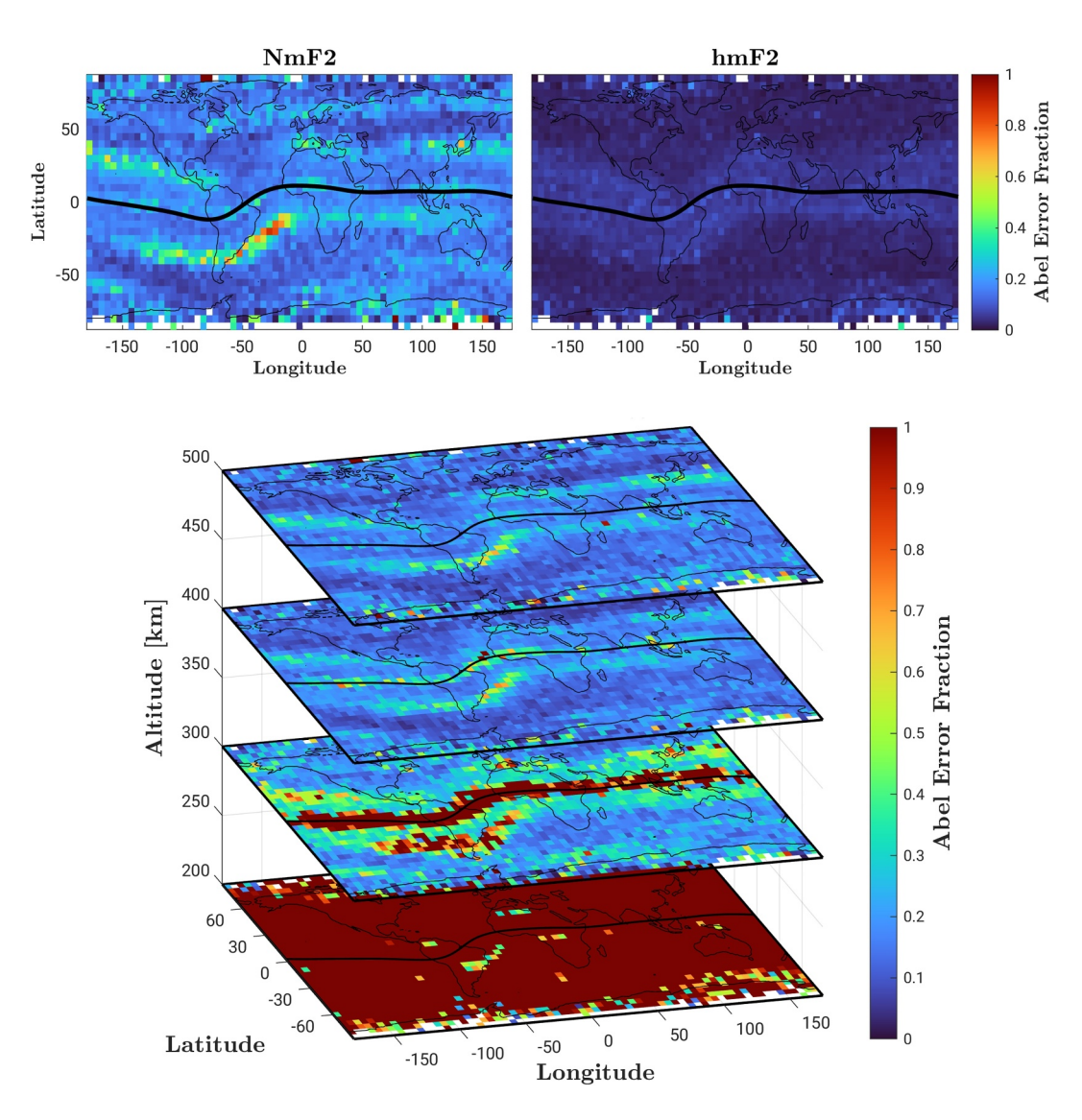


Figure 4. Binned average fractional error due to Abel retrieval, across all local times. Shown for N_mF_2 , h_mF_2 and at each electron density profile altitude. Black line indicates the magnetic equator. Blank regions are due to lack of observation coverage.

failed forward operator, with rejection rates shown in Figure 6a. Negative values are the most common reason for rejection, notably at low altitudes where observation quality is worst. Between 10 and 50% of observations are rejected between 160 and 250 km altitude, with rejection rates considerably improving at higher altitudes. We reject very far off observations using a 10 standard deviation threshold. For OSSE observation counts shown in Figures 6b, 520 km altitude constellations show greater observation counts than the 800 km altitude constellations.

3. OSSE Results

3.1. OSSE Ionospheric Results

First highlighting the quiet period, we show the impact of the first analysis step at UT01 on March 13th in Figure 7, for 300 km altitude. In the top row is the WAM-IPE nature run, where synthetic observations are derived, and the no-assimilation control (identical to the prior here), for electron densities at 300 km altitude. In the middle row are the posterior electron densities for OSSEs 1–4, each containing a single constellation. A first notable bias between WAM-IPE and TIEGCM control is the EIA, where WAM-IPE produces higher magnitudes

DIETRICH ET AL. 8 of 20

15427390, 2024, 8, Downloaded from https://agupubs.onlinelibrary.wiley.com/doi/10.1029/2024SW003958 by University Of Colorado Boulder, Wiley Online Library on [21/06/2025]. See the Terms

ditions) on Wiley Online Library for rules of use; OA articles are governed by the applicable Creativ

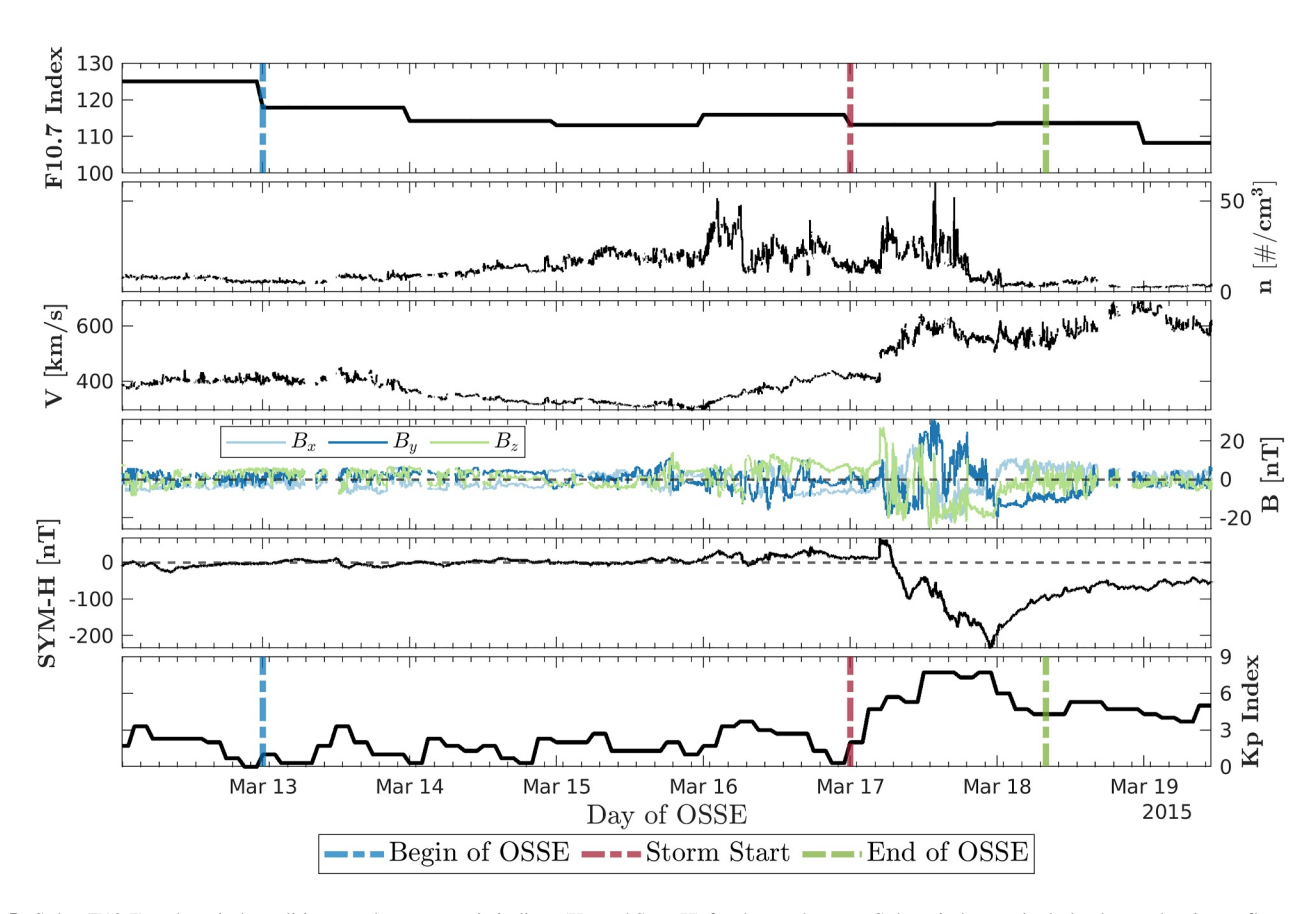


Figure 5. Solar (F10.7), solar wind conditions, and geomagnetic indices (Kp and Sym-H) for the week event. Solar wind states include plasma density, n, flow speed, V, and three magnetic field components, B_x , B_y and B_z . Vertical lines denote the OSSE quiet and storm periods.

and sharper horizontal gradients. High electron densities additionally extend into the night-side for WAM-IPE. In contrast, TIEGCM has a less prominent EIA peak and smoother spatial gradients, stretching for longer length scales, and has EIA peaks westward of WAM-IPE's. Comparing electron density magnitudes between TIEGCM and WAM-IPE, TIEGCM under-represents electron densities on the day-side and over-represents electron densities on the night-side. Assessing the posterior electron density states, seen in the middle row of Figure 7, the analysis step is as expected positively impacting posterior states, such as in increasing the EIA magnitude and better replicating the extension of higher electron density magnitudes into the low-latitude night side. For high inclination constellations 5072 and 8072, electron density magnitudes are noticeably reduced in the night side high-latitudes.

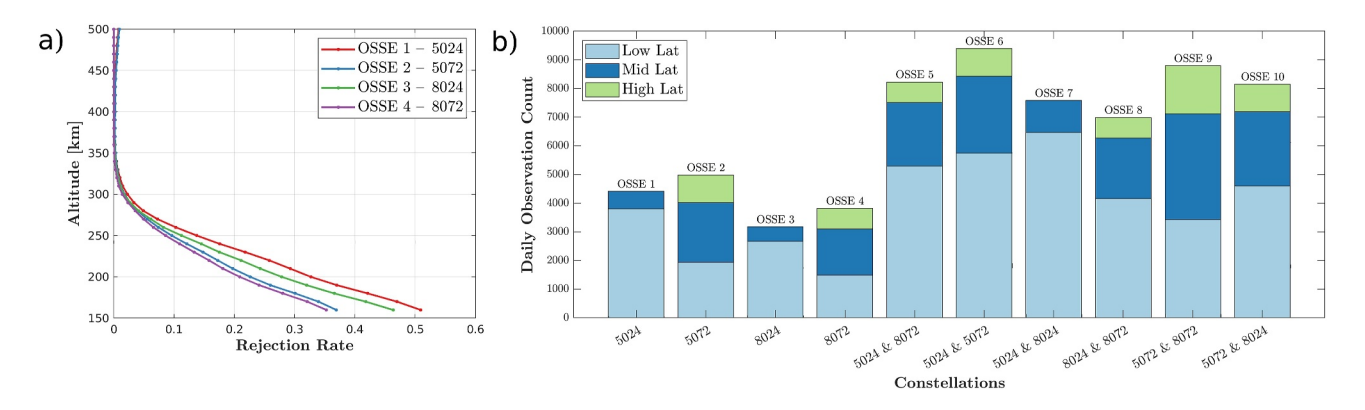


Figure 6. (a) Shows the observation rejection rate as a function of altitude. (b) Shows the daily electron density profile observation count for each OSSE constellation configuration, separated by latitude region.

DIETRICH ET AL. 9 of 20

15427390, 2024, 8, Downloaded from https://agupubs.onlinelibrary.wiley.com/doi/10.1029/2024SW003958 by University Of Colorado Boulder, Wiley Online Library on [21/06/2025]. See

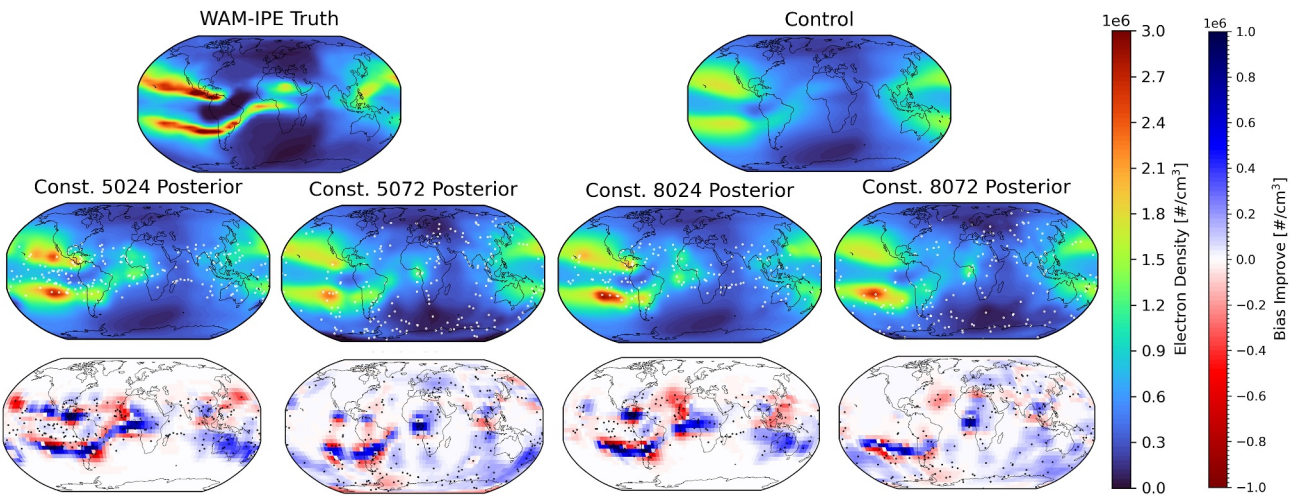


Figure 7. Electron density shown for the nature run, control, and OSSEs 1–4 posteriors at 300 km altitude at UT01 on March 13th, the first analysis step. The middle row shows posterior states, where white points are the assimilated tangent-point observations at 300 km altitude. Bias improvement, shown on bottom row, is illustrated with blue regions providing improvement and red regions worsening.

Illustrating the performance of the analysis update is shown in the bottom row of Figure 7. The analysis bias improvement is defined as

Bias Improve =
$$|\bar{x}^{prior} - x^{NR}| - |\bar{x}^{post} - x^{NR}|$$
 (1)

where $|\mathbf{x}|$ is the element-wise absolute value of mean OSSE state vectors $\bar{\mathbf{x}}^{prior}, \bar{\mathbf{x}}^{post} \in \mathbb{R}^n$ and nature run state vector $\mathbf{x}^{NR} \in \mathbb{R}^n$. Bias improvement is shown in the bottom row of Figure 7, where blue regions indicate improved electron density biases and red regions indicated worsened biases. For state grid point comparisons between the two models, we down-sample WAM-IPE and interpolate as needed to TIEGCM's 5° grid resolution. At locations where WAM-IPE shows large electron density magnitudes, biases overall improve when observations are available. This is most evident for constellations 5024 and 8024 at peak EIA magnitudes. In red regions directly off WAM-IPE's EIA, we see the analysis step worsen biases. Generally, there are red worsen regions where there is a large gradient in WAM-IPE electron densities. More discussion of these worsening regions is addressed in Section 4, and is largely explained by Abel retrieval errors and improper background covariance. A similar figure for the storm period is shown Figure S4 in Supporting Information S1.

As the primary metric to assess OSSE performance, we use the root mean-square error (RMSE) defined as

$$RMSE = \sqrt{\frac{\sum_{j=1}^{N} (x_j^{NR} - \overline{x}_j^{exp})^2}{N}}$$
 (2)

where x_j^{NR} is the *j*th WAM-IPE state, $\overline{x}_j^{\text{exp}}$ is the *j*th ensemble mean OSSE state, and *N* is the total number of states. As RMSE is a magnitude dependent quantity, we separate results into three latitudes regions, where low latitude is between -30° and $+30^{\circ}$, middle latitude is between -30° and -60° as well as 30° and $+60^{\circ}$, and high latitude is below -60° and above 60° . We show results for N_mF_2 , h_mF_2 , TEC, and altitude electron densities. We compare relative posterior RMSE performance against a no-assimilation control.

The N_mF_2 RMSE for all 10 OSSEs is shown in Figure 8 for both quiet and storm periods. At high latitudes, the best performance is seen from OSSE 9 including constellations 5072 and 8072, the constellations with the most high-latitude coverage. As expected, OSSEs 1, 3 and 7 have no high-latitude coverage resulting in negligible impact on high-latitude errors. At low latitudes, OSSE 7, containing constellations 5024 and 8024, performs the best with the highest coverage of observations. Additionally, OSSEs 3 and 4 containing only constellations 5072 and 8072 have the least improvement in errors. At mid-latitudes, the OSSEs containing just constellations 5024 or

DIETRICH ET AL. 10 of 20

15427390, 2024, 8, Downloaded from https://agupubs.onlinelibrary.wiley.com/doi/10.1029/2024SW003958 by University Of Colorado Boulder, Wiley Online Library on [21/06/2025].

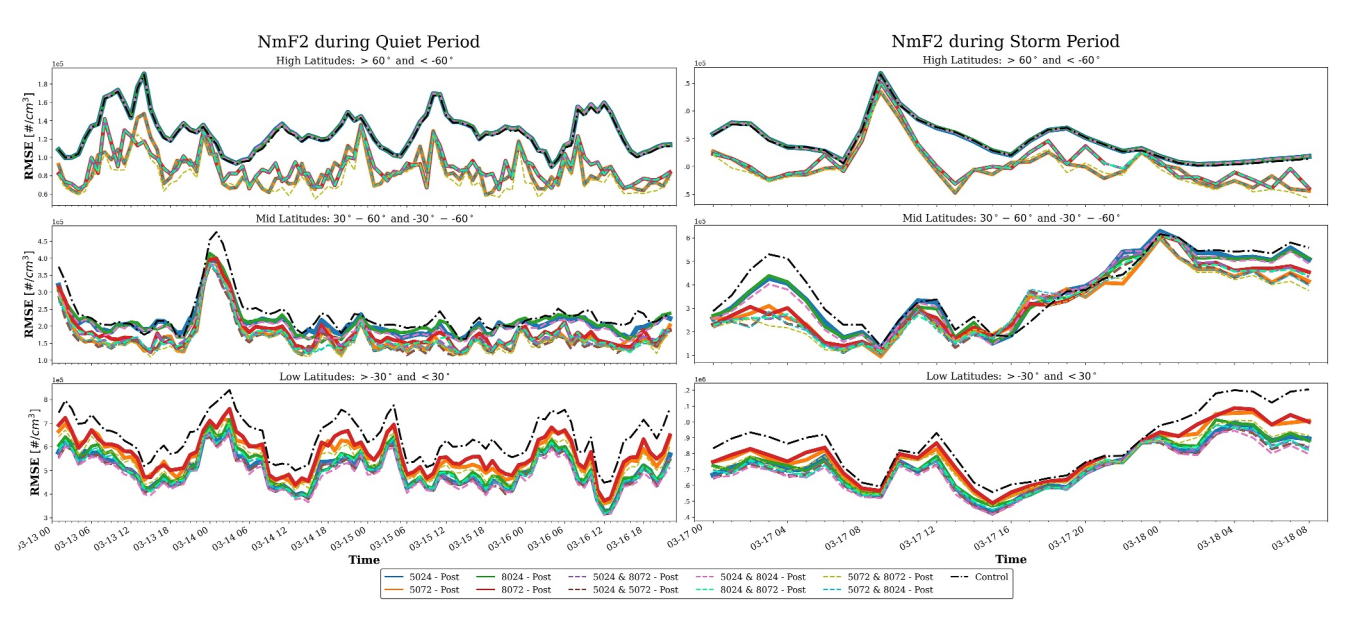


Figure 8. The $N_m F_2$ root mean-square error for each OSSE throughout the quiet period (left) and storm period (right). Solid lines indicate single constellation OSSEs and dashed lines indicate two constellation OSSEs. Performance is assessed compared to a no-assimilation control in the dashed black curve.

8024 have the worst performance, OSSEs 1,3 and 17. High inclination OSSEs show consistent improvement in N_mF_2 RMSE at low-latitudes and in high-latitudes.

The N_mF_2 posterior RMSEs for the storm period are also shown in Figure 8. As with the quiet period at low- and high-latitudes, there is a consistent improvement in RMSE over the control for the storm period, with more observation coverage of a region providing better performance. OSSE 7 with constellations 5024 and 8024 performs the best at low latitudes, and OSSE 9 with constellations 5072 and 8072 performs the best at high latitudes. It is also noted that the control RMSE increases for the storm-period due to increasing model biases between TIEGCM and WAM-IPE.

Further RMSE time-series plots are available Figures S5–S10 in Supporting Information S1. The TEC RMSE time series is shown Figure S5 in Supporting Information S1, showing very similar performance to N_mF_2 RMSEs. h_mF_2 RMSEs are additionally shown in Supporting Plots S6. For h_mF_2 , we see only slight impact to posterior RMSEs as compared with the no-assimilation control. This negligible performance is primarily attributed to a lack of state spread in h_mF_2 , as we expect h_mF_2 observation quality to be very high, see Figure 4. Additional figures, including RMSE at each altitude (200, 300, 400 and 500 km) are available Figures S7–S10 in Supporting Information S1. Altitude RMSEs show similar performance results as the N_mF_2 RMSEs with the exception of 200 km altitude.

Observation comparisons at 200 and 400 km altitude are shown in Figure 9, where these contain all observations from all OSSEs and are shown for the quiet period at a given altitude. Here, WAM-IPE electron density states at EDP observation tangent points are shown against the Abel retrieval, TIEGCM prior and TIEGCM posterior, and separated by latitude region. Each plot is a density map of the observations in each range, normalized by the respective max binned observation count, shown in units of 10^5 cm⁻³. The goodness of fit to the line $x = y, R^2$, and the number of observations, N, are provided for each sub-figure. For 400 km altitude, there is quite good agreement among the WAM-IPE states and Abel retrievals. TIEGCM prior biases are most noticeable at the low latitudes and for the 400 km altitudes there is consistent improvement in posterior agreement and R^2 . Posterior states at 400 km perform best at the high latitudes and worst at low latitudes, likely due to EIA biases. We see all Abel retrieval values of R^2 greater than or equal to 0.78. Observation comparisons for 300 and 500 km altitudes are shown Figure S11 in Supporting Information S1 and show similar results to 400 km altitude.

In the left sub-figure of Figure 9 for 200 km altitude, we see very different results. For all latitude regions, the Abel retrieval and TIEGCM prior and posterior are all severely underbiased to WAM-IPE nature run electron densities. Still, we do see improvement in agreement for posterior states at the middle and high latitudes, while the

DIETRICH ET AL. 11 of 20

15427390, 2024, 8, Downloaded from https://agupubs.onlinelibrary.wiley.com/doi/10.1029/2024SW003958 by University Of Colorado Boulder, Wiley Online Library on [21/06/2025]. See the Term

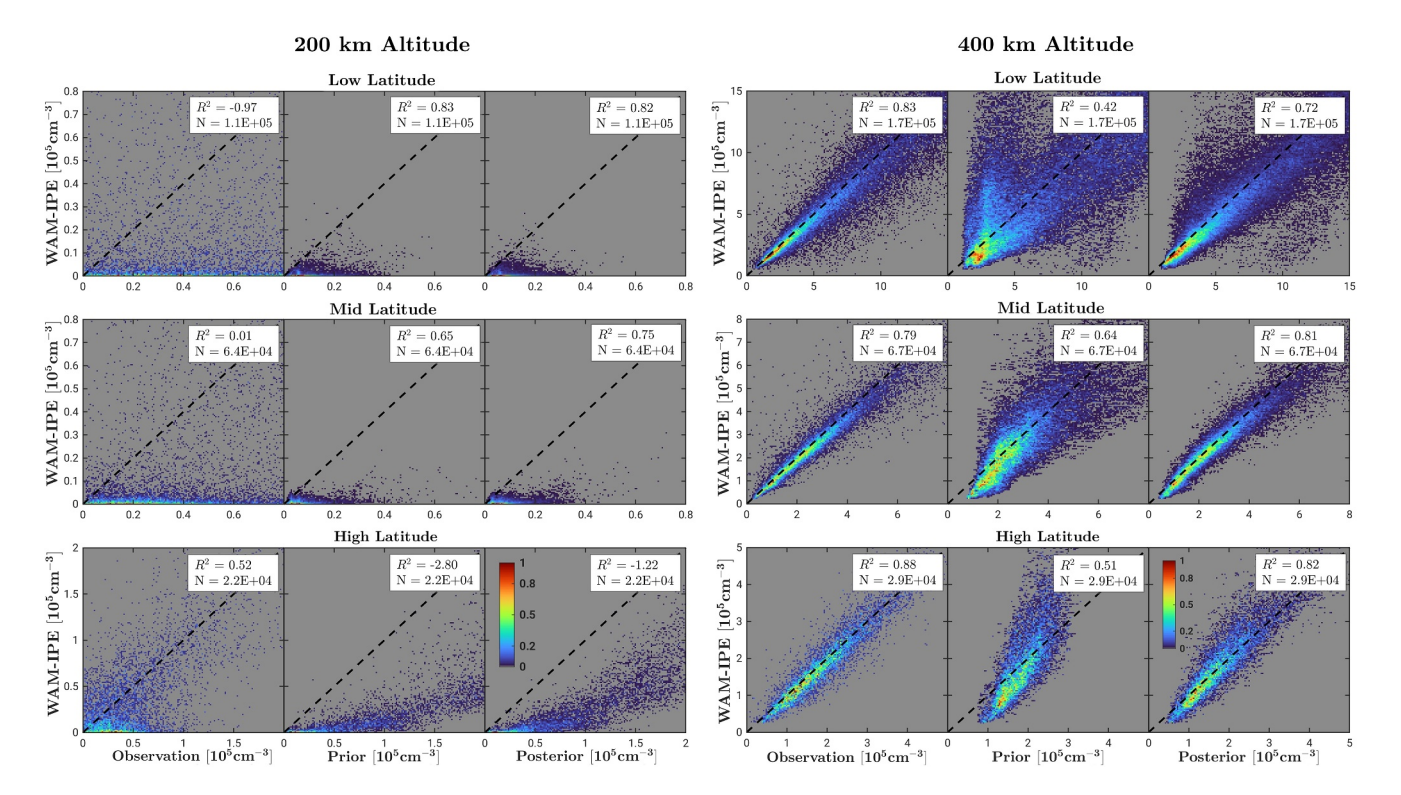


Figure 9. Comparison of electron density observations at given altitudes (200 and 400 km), with the nature run WAM-IPE state shown against the Abel retrieval, TIEGCM prior and TIEGCM posterior states. Density heat maps are shown, with counts normalized by the max bin count for that subplot. Units are all in 10⁵ cm⁻³.

200 km low latitudes show worsening error. The low and middle latitudes priors have surprising good R^2 values, due to many states being very low magnitude (not very visible on this plot axis scale), while the Abel retrieval at low latitudes has a negative R^2 value.

3.2. Ranking Metric

To further quantify relative OSSE performance, we devise a simple high-level ranking metric. Using the time series of RMSEs calculated for N_mF_2 , h_mF_2 , TEC and altitude electron densities, each OSSE is ranked for each hour. The 10 OSSEs are ordered and ranked according to each OSSE's RMSE, 1 through 10, with 1 having the lowest error (best performance) and 10 having the highest error (worst performance). Averaging hourly OSSE ranks over the whole experiment period then gives the ranking metric.

The vertically integrated TEC ranking metric is shown in Figure 10 for the three latitude bins and globally, for both the quiet and storm periods. Table cells are color-coated with deep green indicating the best performance (close to 1) and deep red indicating worst performance (close to 10). For low latitudes, OSSE 7 (5024 and 8024) performs the best with the highest coverage of low latitudes. For high latitudes, OSSE 9 (5072 and 8072) performs the best with the highest coverage in that respective region. OSSEs that mix high and low inclination constellations, OSSE 5, 6, 8 and 10, generally do well across the board. OSSE performances are similar for quiet and storm conditions as most quiet and storm rankings are within a rank of 1. For global rankings, these typically reflect performance at the low and mid-latitudes, where the largest electron density magnitudes are present and thus dominate RMSEs. Additional ranking metric tables are available for $N_{\rm m}F_2$, $h_{\rm m}F_2$ and electron density at altitudes 200, 300, 400 and 500 km Figures S12, S13 and S14 in Supporting Information S1. It is noted that TEC, $N_{\rm m}F_2$ and 300–500 km altitude ranking values all indicated similar results.

To explain ranking metrics performance, we collect all the rankings for the quiet period at 200, 300, 400 and 500 km electron density altitudes (Figure S12 in Supporting Information S1) and plot them against their daily average observation count, shown in Figure 11. The left sub-figure shows results collected for altitudes 300, 400 and 500 km, and the right shows rankings for 200 km, also splitting for low, mid and high latitudes. Very simply, where we have more observation, we see better OSSE performance with lower metric ranks as shown with a

DIETRICH ET AL. 12 of 20

15427390, 2024, 8, Downloaded from https://agupubs.onlinelibrary.wiley.com/doi/10.1029/2024SW003958 by University Of Colorado Boulder, Wiley Online Library on [21/06/2025]. See the Terms

		Low Lat	Mid Lat	High Lat	Global	Low Lat	Mid Lat	High Lat	Global
Experiment Name	Constellations	Quiet				Storm			
OSSE 1	5024	4.98	9.31	8.8	5.85	5.7	8.42	8.58	6.79
OSSE 2	5072	9.09	5.37	3.97	9.03	7.97	4.09	3.06	7.09
OSSE 3	8024	6.8	9.28	8.96	7.24	5.82	6.94	9.06	6.48
OSSE 4	8072	9.91	6.9	4.27	9.91	9.67	5.18	4.55	9.03
OSSE 5	5024 & 8072	3.6	4	4.84	3.05	4.91	6.3	5.42	4.88
OSSE 6	5024 & 5072	2.27	2.55	4.37	1.64	3.09	4.7	3.85	2.76
OSSE 7	5024 & 8024	1.34	7.71	8.93	2.79	2.21	7.82	8.73	4.42
OSSE 8	8024 & 8072	5.43	4.53	4.55	4.93	4.85	5.15	5.48	4.82
OSSE 9	5072 & 8072	7.83	2.31	2.19	7.43	7.33	2.82	2.45	5.94
OSSE 10	5072 & 8024	3.77	2.81	4.13	3.13	3.45	3.58	3.82	2.79

Figure 10. OSSE ranking metric for total electron content. Rankings are averaged over the quiet period defined from March 13th UT01 to March 16th UT022 and averaged over the storm period defined from March 17th UT00 to March 18th UT08. Values close to 1 indicate the best performance and values close to 10 indicate the worst performance.

strong negative correlation. This finding holds for all regions except for one: 200 km altitude at low latitudes. These values are reflected Figure S12 in Supporting Information S1 where worsening ranking is seen for 200 km in OSSEs, as well as in Figure 9 at 200 km with little agreement between WAM-IPE states and Abel retrieved EDPs. Regardless, we still do see improvement in the ranking metric at 200 km altitudes for mid- and high-latitudes, same as all other regions improving performance with greater observation coverage.

Quiet Period Constellation Performance

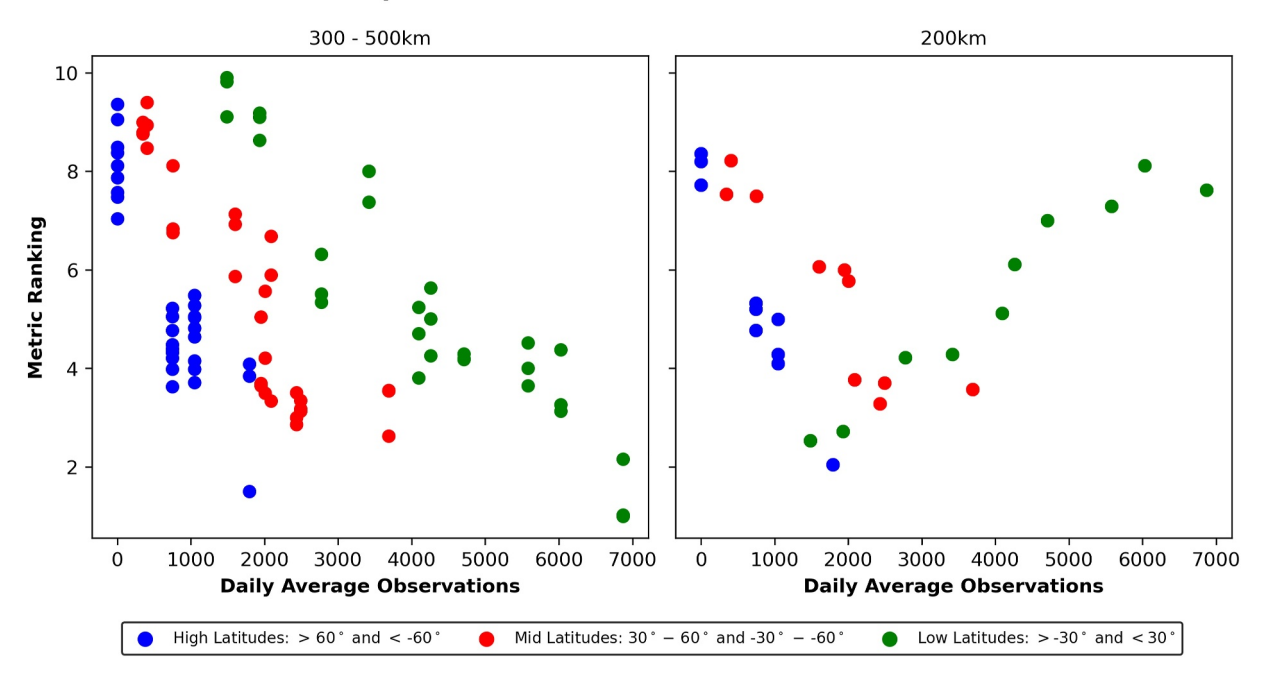


Figure 11. The relationship between the latitude observation counts shown in Figure 6b and the ranking metrics Figure S12 in Supporting Information S1. Again noting that one indicates the best ranking and 10 indicates the worst ranking. All show a negative correlation (improvement with more observations) with the exception of 200 km at low latitudes.

DIETRICH ET AL. 13 of 20

15427390, 2024, 8, Downloaded from https://agupubs.onlinelibrary.wiley.com/doi/10.1029/2024SW003958 by University Of Colorado Boulder, Wiley Online Library on [21/06/2025]

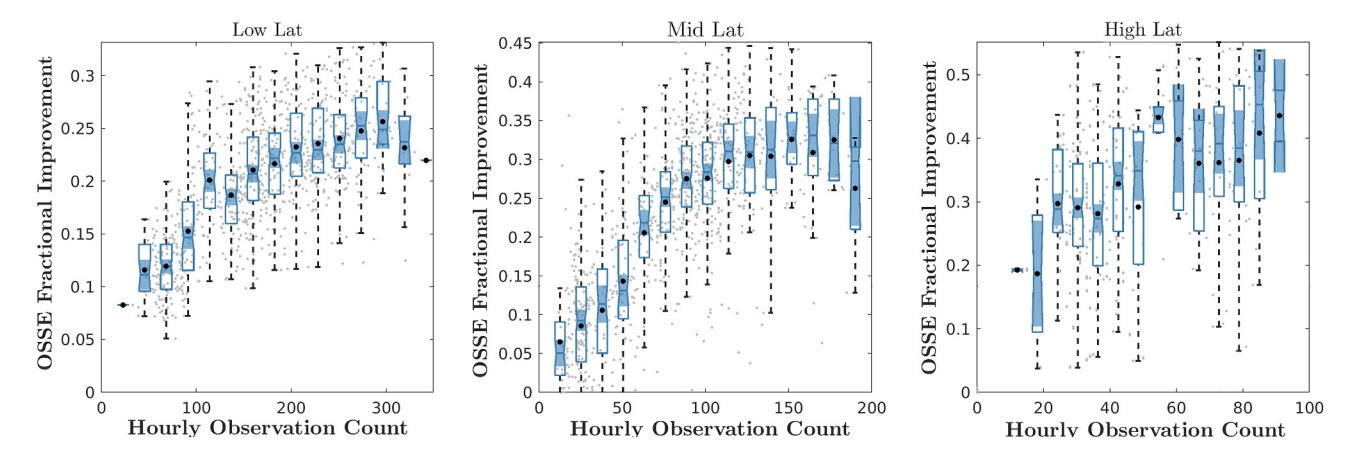


Figure 12. OSSE $N_m F_2$ root mean-square error (RMSE) fractional improvement over the control as a function of observation count, defined in Equation 3. Calculated for the entire $N_m F_2$ grid RMSE within each latitude band. Mean improvement (black dots) and notched box plots are averaged over count bins of all samples (grey dots). Non-overlapping shaded regions indicate the significant difference between medians (5% confidence).

A couple of additional results are as follows. First, we see more observations from the 520 km altitude constellations than the 800 km altitude constellations, and this directly corresponds to better ranking metrics for these OSSEs. With this, it is arguable that OSSE 6 with 5024 and 5072 is the best performing OSSE (as reflected in the global ranking metric in Figure 10). We see constellation 8024 have 27% less profiles than constellation 5024; we see constellation 8072 have 24% less profiles than constellation 5072. The differences is likely explained by the shorter orbit period of the 520 km altitude constellations, enabling more limb passes and RO events. Secondly, OSSE 9 with 5072 and 8072 performs poorly for low latitude observations, as one might expect; however from Figure 6, OSSE 9 performs worse than OSSEs 1 (5024) and 3 (8024) with comparable low-latitude coverage. This worse performance can potentially be explained by larger observation errors that the high inclination constellations show at low-latitudes, as illustrated most evidently in the bottom left panel of Figure 3. Thus a combination of a low- and high-inclination constellation provides the best global coverage.

3.3. Observation Performance Limit

An additional question raised when designing an observing system and adding more observations: what is the potential performance limit? We define a "performance limit" as the point when assimilating more observations plateaus improving OSSE errors. To address this question with available OSSE results, we compute the RMSE for all grid points for the low-, mid- and high-latitude regions of each OSSE, as well as for the control. We then define the OSSE fractional improvement over the control as

Fractional Improvement =
$$\frac{RMSE_{cntrl} - RMSE_{exp}}{RMSE_{cntrl}}$$
 (3)

this is done for every hour of the OSSE and all 10 OSSEs. Next binning over hourly observation counts we show the mean and notched box plot for the N_mF_2 RMSEs in Figure 12. For the low- and mid-latitudes, there is a steady improvement in performance with more observations and a visible leveling off, as the improvement is no longer statistically significant at the peak observation counts. It is noted for the end points of each latitude region, shaded regions have very small or very large spread due to a limited number of samples. For high latitudes, the results are more noisy as we have less samples due having only two constellations with high-latitude coverage. We see a positive trend in the high-latitude fractional improvement that does not appear to plateau. Results for TEC show very similar results to N_mF_2 (Figure S15 in Supporting Information S1), and h_mF_2 fractional improvement are less consistent (Figure S16 in Supporting Information S1). Further study is needed to investigate the cause of this performance limit, such as due to observation errors, background covariance, localization and other DA parameters, model errors, model resolution, or observation spatial density.

DIETRICH ET AL. 14 of 20

4. Discussion

Returning to the initial question we first posed as to what constellation configuration is best: it depends. Simply put, with more observation coverage in a given region, we gain better ionosphere specification, with a combination of a low- and high-inclination constellation providing the best global coverage. Therefore, designing an RO constellation observing system depends on what regions we desire to study or monitor.

Fully simulating the Abel inversion retrieval for EDP observations allows us to evaluate the impact of Abel inversion errors within a DA framework, as compared with studies such as Hsu et al. (2014), Lee et al. (2013) that only perturbed using Gaussian errors. Previously documented Abel inversion errors are evident, notably at the low latitudes and low altitudes (Tsai et al., 2001), and their resulting in poor analysis updates. Abel inversion particularly has trouble reproducing the low electron densities in "plasma caves" beneath the EIA crests (Liu et al., 2010; Yue et al., 2010), as this is the one the one region (200 km, low latitude) we see the DA have negative impact on electron density states. These were also expected from Figure 4 where there are considerably high Abel retrieval errors. Nevertheless, we do see positive impact for 200 km altitudes at the mid- and high-latitudes. Additionally as we move to higher altitudes, we see observations consistently provide positive data impact.

OSSE results suggest this region of very low electron densities is likely an inherent limitation of RO and the Abel inversion technique. As we move to lower altitudes, the radio signal passes becoming increasing longer, comprising more of the ionosphere and yielding larger slant TEC observations. The Abel retrieved EDPs cannot resolve the WAM-IPE's low electron densities using large TEC observations, especially if the spherical symmetry assumption is increasingly broken, adding more observation noise. We also see many negative observations in this region, reducing data available for assimilation. Therefore we see RO EDPs to not be useful for ionospheric specification in this low latitude, low altitude region, supporting the conclusions of Lee et al. (2012).

To detail poor EDP performance, we highlight two assimilated profiles shown in Figure 13. We focus on the worsening regions of constellation 5024 from Figure 7. We show the WAM-IPE nature run, Abel retrieval, and the TIEGCM prior and posterior at profile locations.

One source of poor analysis updates come from DART-TIEGCM, exhibited by profile (a) of Figure 13. At this location, there is good agreement between the Abel retrieved EDP (and its assigned 1 standard deviation (std) uncertainty) and the WAM-IPE nature run. The RO event details of profile (a) is additionally shown in Figure S18 in Supporting Information S1 where the black tangent points are close to vertical and the red RO ray passes align with the EIA gradients. This observation point is within the EIA peak electron density, and as the EAKF locally updates states using the ensemble background covariance, an over-correction is performed for grid points off WAM-IPE's EIA structure. The regional impact of this observation is shown in the bottom plot of Figure 13, including the nature run WAM-IPE state at 300 km, TIEGCM's background electron density correlation and the observation increment. TIEGCM shows high background correlations extending beyond WAM-IPE's sharper electron density gradient, and the update is very much defined by the isotropic GC localization. This poor update underscore the importance of having a good background covariance, and is a necessary filter feature for global specification. Many studies have been devoted to improving the local update impact, either through improved background covariance or through localization (e.g., Forsythe et al., 2020; Hsu et al., 2018; Lin et al., 2015; Zhang et al., 2023).

Another source of poor analysis updates, one very much a focus of this study, come from Abel inversion errors, shown at point (b) of Figure 13. At this location, the prior EDP has fine agreement with WAM-IPE; however, the Abel inverted EDP is considerably more biased, and we see worse posterior error. This profile deviates from the typical Chapman function, instead showing a double peak structure in both the EDP observation and WAM-IPE RO tangent points. A view of this profile and the WAM-IPE states are shown in Figure S17 in Supporting Information S1, where the tangent points' quasi-vertical profile at high altitudes includes higher magnitude electron densities. The RO event geometry for profile (b) is also shown in Figure S18 in Supporting Information S1, where the tangent points span a large horizontal region. There is a large electron density gradient that the RO view angle crosses over two distinct ionospheric regions, introducing sizable errors into the Abel inversion retrieval. Ideally, this observation profile should be flagged for quality control and not assimilated, or alternatively the observation uncertainty should be considerably increased to more sufficiently account for the Abel inversion error.

It is noted as a caveat that the devised ranking metrics only provides a big-picture view of the relative OSSE results. These rankings do not indicate the magnitude of the relative OSSE performance, and should be viewed in

DIETRICH ET AL. 15 of 20

15427390, 2024, 8, Downloaded from https://agupubs.onlinelibrary.wiley.com/doi/10.1029/2024SW003958 by University Of Colorado Boulder, Wiley Online Library on [21/06/2025]. See the Terms and Conc

(b)

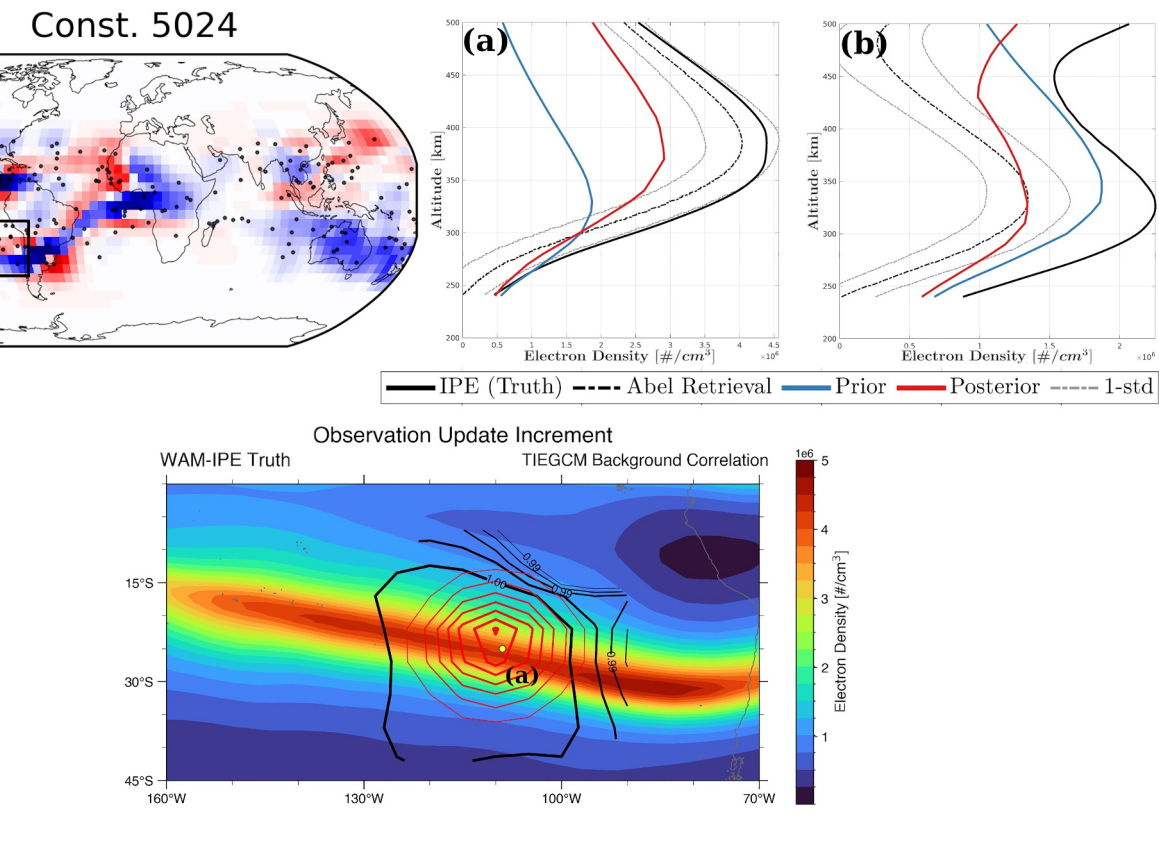


Figure 13. Highlighting two electron density profiles (EDPs) introducing poor analysis updates. Shown using first analysis step of constellation 5024 (same as in Figure 7). EDP (a) highlights poor background covariance, EDP (b) highlights large Abel inversion error. Bottom contour plot shows the WAM-IPE electron density at 300 km, and the observation increment (red) and TIEGCM background correlation (black).

conjunction with the RMSE time series plots to gain a full perspective. Regardless, conclusions from these rankings generally support the findings from the RMSE time-series. Additionally assessing errors through RMSE and with parameters TEC and N_mF_2 can simplify the global impression of ionosphere specification. These metrics are decidedly magnitude dependent, sometimes representing only the highest magnitude locations, for example, the EIA or F_2 peak. The altitude profile of the electron density can be very important for space weather influences, making ionospheric specification a three-dimensional problem needing to be address through multiple metrics.

We focus in this study on the relative performance of all OSSEs, and the filter performed well enough for assessment. Filter features such as tuned localization, implementing inflation, and better ensemble initialization with more realistic geomagnetic forcing would all help to improve data impact of the synthetic EDPs. One evident source of poor impact is with the lack of h_mF_2 spread in TIEGCM, as previously noted in Lee et al. (2012), that causes h_mF_2 improvement to be considerably less than expected given their low errors.

Another large restriction in filter performance was achieving sustained RMSE improvement from using a coupled I-T model due to plasma states have limited memory in the system. Non-updated neutral states in TIEGCM quickly rebound posterior plasma states back to control states in the forecast step, showing only a 1–2 hr system memory. Previous studies have shown plasma forecasting only on the order of hours with ionosphere assimilation in coupled I-T models (Chartier et al., 2013; Jee et al., 2007). Neutral states have a longer forecasting memory (Chartier et al., 2013), and specifying neutral states such as oxygen composition have been shown to greatly improve plasma forecasting (Hsu et al., 2014). This would help the system to retain plasma RMSE improvements when forecasting and see greater OSSE performance. Another possibility not included in this study is the potential to estimate neutral states using the EDP observations, and has been shown to have positive impact for composition, neutral temperature and neutral winds (Dietrich et al., 2022; Matsuo & Hsu, 2021).

Accounting for realistic Abel inversion and forecast model errors in this study underscores the need for more complete EDP error quantification and observation quality control. There still remains work needed to fully

DIETRICH ET AL. 16 of 20

quantify Abel inversion errors, and quantify their impacts from breakdowns in the spherical symmetry assumption. In this study there are two main error sources included in these OSSEs: errors from Abel inversion and errors within the DART-TIEGCM DA framework, and it is challenging to fully deconvolve these two error sources. Future OSSE work could apply the same OSSE set-up while also running equivalent OSSEs with synthetic EDPs directly sampled at WAM-IPE locations, enabling direct comparisons of error impacts and more complete quantification of Abel inversion errors. Abel error fitting over altitude, magnetic latitude and local time, as in Yue et al. (2010), Liu et al. (2010), was shown to not be sufficient in some cases. Additional error analysis capturing exactly how the spherical symmetry assumption is being broken is needed by analyzing the radio ray paths taken through the ionosphere. Better quantification of these Abel errors should improve DA performance in negatively impacted regions, and provide means for better observation quality control. Further, more advanced Abel inversion algorithms have improved low altitude observations errors and improved their DA impact (e.g., Chou et al., 2017; Pedatella et al., 2015; Tulasi Ram et al., 2016; Wu, 2018) and were not included in this study.

5. Conclusions

To inform future RO constellation mission planning and design, this study uses a comprehensive OSSE approach to evaluate the ionospheric specification impact of assimilating RO EDPs into a coupled I-T model. We perform 10 OSSE configurations to evaluate four base hypothetical RO constellations. These RO constellations are modeled after F3/C and F7/C2, at either 24° or 72° inclination and at either 520 or 800 km altitude orbits. Each OSSE's relative performance is evaluated through multiple metrics during the St. Patrick's Day storm on March 13–18, 2015, including quiet and storm-time conditions, by using the DART-TIEGCM and a nature run simulation provided by WAM-IPE. This study is the first ionospheric OSSE study to comprehensively and realistically account for forecast model and observation errors by using a distinct nature run simulation and forecast model, as well as retrieving synthetic EDP observations from the WAM-IPE nature run with an extensive Abel inversion procedure.

Overall, better spatial coverage of EDP observations from a given RO constellation design corresponds to a better OSSE performance. For low-inclination constellations with greater low-latitude coverage, the best performance is obtained for the low latitude ionosphere, and likewise for high-inclination constellations the best performance is achieved for the high latitude ionosphere. The increased spatial coverage of EDPs directly corresponding to improved results is best reflected in a ranking metric, with higher observation counts seen for the 520 km altitude constellations, arguably making OSSE 6 (5024 and 5072) the best performing OSSE. This combination of a low-and high-inclination constellation additionally provides the best global coverage. Consistent posterior improvement is seen at all latitudes for altitudes 300–500 km, demonstrating evident benefits to EDP assimilation. A performance limit is also conceivably illustrated for two 6-satellite constellations, and further study is needed to uncover its causes and validity.

Another notable finding is the limitations of RO EDP data impact on the dayside equatorial region at low altitudes. DA impact in this region is negatively impacted by worsening Abel inversion errors due to both breakdowns in the spherical symmetry as well as RO's inherent shortcoming in accurately retrieving very low, low altitude plasma densities. Additional large retrieval errors are seen when vertical plasma density structures deviate from the typical Chapman function, such as double peaked EDPs.

Ultimately, RO EDPs offer a unique, three-dimensional global ionospheric perspective advantageous for global ionospheric specification. While Abel retrieval and uncertainty quantification may still be improved, as considered in the discussion, RO EDPs offer clear operational space weather benefits for the upper atmosphere. Further assessment of space weather observing systems using comprehensive OSSE studies will considerably enhance future observation integration into DA systems, as well as greatly aid in future constellation design.

Data Availability Statement

Software tools used for the work are all publicly available. The Whole Atmosphere Model Ionosphere Plasmasphere Electrodynamics (WAM-IPE) software was developed by the NOAA Space Weather Prediction Center and available from https://github.com/CU-SWQU/GSMWAM-IPE. The Data Assimilation Research Testbed (DART) software was developed by the National Center for Atmospheric Research (NCAR) Computational and Information Systems Lab and available from http://dart.ucar.edu. A tutorial for DART is available here: https://dart.ucar.edu. A tutorial for DART is available here:

DIETRICH ET AL. 17 of 20

1029/2024SW003958 by University Of Colorado Boulder, Wiley Online Library on [21/06/2025]. See the Terms

dart.ucar.edu/tutorials/. The Thermosphere Ionosphere Electrodynamics General Circulation Model (TIEGCM) software was developed by the NCAR High Altitude Observatory and available from http://www.hao.ucar.edu/modeling/tgcm/tie.php. Abel inversion algorithm code was developed by the COSMIC Data Analysis and Archive Center (CDAAC) and available from https://cdaac-www.cosmic.ucar.edu/. The Observing System Simulation Experiment data used for the experiment ensembles, control and nature runs used in this study are available at Dietrich (2024).

Acknowledgments

This work was supported by the National Ocean and Atmospheric Administration (NOAA) Office of Space Weather Observations (SWO), through the UCAR subaward SUBAWD00003038, as well as the NSF award AGS 1848544 (CAREER) and the NASA award 80NSSC23K1631 (FINESST) to the University of Colorado Boulder. Chi-Yen Lin and Charles Lin are partly supported by Taiwan Space Agency under TASA-S-1120747. The authors thank Irfan Azeem and Dimitrios Vassiliadis at the NOAA SWO for their guidance and feedback on the project. The authors would like to acknowledge highperformance computing support from Cheyenne (doi:10.5065/D6RX99HX) provided by NCAR's Computational and Information Systems Laboratory, sponsored by the National Science Foundation. The authors thank the reviewers for their helpful feedback.

References

- Akmaev, R. A. (2011). Whole atmosphere modeling: Connecting terrestrial and space weather. *Reviews of Geophysics*, 49(4). https://doi.org/10. 1029/2011rg000364
- Anderson, J. L. (2001). An ensemble adjustment Kalman filter for data assimilation. *Monthly Weather Review*, 129(12), 2884–2903. https://doi.org/10.1175/1520-0493(2001)129(2884:AEAKFF)2.0.CO:2
- Anderson, J. L., & Collins, N. (2007). Scalable implementations of ensemble filter algorithms for data assimilation. *Journal of Atmospheric and Oceanic Technology*, 24(8), 1452–1463. https://doi.org/10.1175/jtech2049.1
- Anderson, J. L., Hoar, T., Raeder, K., Liu, H., Collins, N., Torn, R., & Avellano, A. (2009). The data assimilation research testbed: A community facility. *Bulletin of the American Meteorological Society*, 90(9), 1283–1296. https://doi.org/10.1175/2009BAMS2618.1
- Andersson, E., & Masutani, M. (2010). Collaboration on observing system simulation experiments (Joint OSSE). ECMWF Newsletter, 123, 14-16
- Angling, M. J., Nogués-Correig, O., Nguyen, V., Vetra-Carvalho, S., Bocquet, F. X., Nordstrom, K., et al. (2021). Sensing the ionosphere with the spire radio occultation constellation. *Journal of Space Weather and Space Climate*, 11(2001), 56. https://doi.org/10.1051/swsc/2021040
- Anthes, R. A., Bernhardt, P. A., Chen, Y., Cucurull, L., Dymond, K. F., Ector, D., et al. (2008). The COSMIC/FORMOSAT-3 mission: Early results. Bulletin of the American Meteorological Society, 89(3), 313–334. https://doi.org/10.1175/BAMS-89-3-313
- Anthes, R. A., Shao, H., Marquardt, C., & Ruston, B. (2023). Radio Occultation Modeling Experiment (ROMEX) framework. Retrieved from https://irowg.org/ro-modeling-experiment-romex/#
- Chartier, A. T., Jackson, D. R., & Mitchell, C. N. (2013). A comparison of the effects of initializing different thermosphere-ionosphere model fields on storm time plasma density forecasts. *Journal of Geophysical Research: Space Physics*, 118(11), 7329–7337. https://doi.org/10.1002/
- Chartier, A. T., Matsuo, T., Anderson, J. L., Collins, N., Hoar, T. J., Lu, G., et al. (2016). Ionospheric data assimilation and forecasting during storms. *Journal of Geophysical Research: Space Physics*, 121(1), 764–778. https://doi.org/10.1002/2014JA020799
- Chen, C. H., Lin, C. H., Matsuo, T., Chen, W. H., Lee, I. T., Liu, J. Y., et al. (2016). Ionospheric data assimilation with thermosphere-ionosphere-electrodynamics general circulation model and GPS-TEC during geomagnetic storm conditions. *Journal of Geophysical Research: Space Physics*, 121(6), 5708–5722. https://doi.org/10.1002/2015JA021787
- Cherniak, I., Zakharenkova, I., Braun, J., Wu, Q., Pedatella, N., Schreiner, W., et al. (2021). Accuracy assessment of the quiet-time ionospheric F2 peak parameters as derived from COSMIC-2 multi-GNSS radio occultation measurements. *Journal of Space Weather and Space Climate*, 11, 1–14. https://doi.org/10.1051/swsc/2020080
- Chou, M. Y., Lin, C. C., Tsai, H. F., & Lin, C. Y. (2017). Ionospheric electron density inversion for global navigation satellite systems radio occultation using aided Abel inversions. *Journal of Geophysical Research: Space Physics*, 122(1), 1386–1399. https://doi.org/10.1002/2016JA023027
- Dietrich, N. (2024). Evaluating radio occultation (RO) constellation designs using observing system simulation experiments (OSSEs) for ionospheric specification. https://doi.org/10.17605/OSF.IO/EM7FK
- Dietrich, N., Matsuo, T., & Hsu, C.-T. (2022). Specifying satellite drag through coupled thermosphere-ionosphere data assimilation of radio occultation electron density profiles. Space Weather, 20(8), https://doi.org/10.1029/2022SW003147
- Errico, R. M., Yang, R., Privé, N. C., Tai, K.-S., Todling, R., Sienkiewicz, M. E., & Guo, J. (2013). Development and validation of observing-system simulation experiments at NASA's global modeling and assimilation office. *Quarterly Journal of the Royal Meteorological Society*, 139(674), 1162–1178. https://doi.org/10.1002/qj.2027
- Fong, C. J., Chu, C. H., Lin, C. L., & Curiel, A. D. S. (2019). Toward the most accurate thermometer in space: FORMOSAT-7/COSMIC-2 constellation. *IEEE Aerospace and Electronic Systems Magazine*, 34(8), 12–20. https://doi.org/10.1109/MAES.2019.2924133
- Forsythe, V. V., Azeem, I., Blay, R., Crowley, G., Gasperini, F., Hughes, J., et al. (2021). Evaluation of the new background covariance model for the ionospheric data assimilation. *Radio Science*, 56(8), 1–10. https://doi.org/10.1029/2021RS007286
- Forsythe, V. V., Azeem, I., & Crowley, G. (2020). Ionospheric horizontal correlation distances: Estimation, analysis, and implications for ionospheric data assimilation. *Radio Science*, 55(12), 1–14. https://doi.org/10.1029/2020RS007159
- Gaspari, G., & Cohn, S. E. (1999). Construction of correlation functions in two and three dimensions. Quarterly Journal of the Royal Meteorological Society, 125(554), 723–757. https://doi.org/10.1256/smsqj.55416
- Hajj, G. A., & Romans, L. J. (1998). Ionospheric electron density profiles obtained with the Global Positioning System: Results from the GPS/MET experiment. Radio Science, 33(1), 175–190. https://doi.org/10.1029/97rs03183
- He, J., Yue, X., Wang, W., & Wan, W. (2019). EnKF ionosphere and thermosphere data assimilation algorithm through a sparse matrix method. Journal of Geophysical Research: Space Physics, 124(8), 7356–7365. https://doi.org/10.1029/2019JA026554
- Hoffman, R. N., & Atlas, R. (2016). Future observing system simulation experiments. Bulletin of the American Meteorological Society, 97(9), 1601–1616. https://doi.org/10.1175/bams-d-15-00200.1
- Hsu, C. T., Matsuo, T., & Liu, J. Y. (2018). Impact of assimilating the FORMOSAT-3/COSMIC and FORMOSAT-7/COSMIC-2 RO data on the midlatitude and low-latitude ionospheric specification. *Earth and Space Science*, 5(12), 875–890. https://doi.org/10.1029/2018EA000447
- Hsu, C.-T., Matsuo, T., Wang, W., & Liu, J.-Y. (2014). Effects of inferring unobserved thermospheric and ionospheric state variables by using an Ensemble Kalman filter on global ionospheric specification and forecasting. *Journal of Geophysical Research: Space Physics*, 119(11), 9256–9267. https://doi.org/10.1002/2014JA020390
- Jee, G., Burns, A. G., Wang, W., Solomon, S. C., Schunk, R. W., Scherliess, L., et al. (2007). Duration of an ionospheric data assimilation initialization of a coupled thermosphere-ionosphere model. Space Weather, 5(1), 1–11. https://doi.org/10.1029/2006SW000250
- Kelley, M. C., Wong, V. K., Aponte, N., Coker, C., Mannucci, A. J., & Komjathy, A. (2009). Comparison of COSMIC occultation-based electron density profiles and TIP observations with Arecibo incoherent scatter radar data. *Radio Science*, 44(4). https://doi.org/10.1029/2008rs004087

DIETRICH ET AL. 18 of 20



- 10.1029/2024SW003958
- Kodikara, T., Zhang, K., Pedatella, N. M., & Borries, C. (2021). The impact of solar activity on forecasting the upper atmosphere via assimilation of electron density data. *Space Weather*, 19(5), e2020SW002660. https://doi.org/10.1029/2020SW002660
- Kursinski, E. R., Hajj, G. A., Schofield, J. T., Linfield, R. P., & Hardy, K. R. (1997). Observing Earth's atmosphere with radio occultation measurements using the global positioning system. *Journal of Geophysical Research*, 102(19), 23429–23465. https://doi.org/10.1029/ 97id01569
- Lee, İ. T., Matsuo, T., Richmond, A. D., Liu, J. Y., Wang, W., Lin, C. H., et al. (2012). Assimilation of FORMOSAT-3/COSMIC electron density profiles into a coupled thermosphere/ionosphere model using ensemble Kalman filtering. *Journal of Geophysical Research*, 117(10), 1–11. https://doi.org/10.1029/2012JA017700
- Lee, I. T., Tsai, H. F., Liu, J. Y., Lin, C. H., Matsuo, T., & Chang, L. C. (2013). Modeling impact of FORMOSAT-7/COSMIC-2 mission on ionospheric space weather monitoring. *Journal of Geophysical Research: Space Physics*, 118(10), 6518–6523. https://doi.org/10.1002/jgra.
- Lei, J., Syndergaard, S., Burns, A. G., Solomon, S. C., Wang, W., Zeng, Z., et al. (2007). Comparison of COSMIC ionospheric measurements with ground-based observations and model predictions: Preliminary results. *Journal of Geophysical Research*, 112(7), 1–10. https://doi.org/10. 1029/2006JA012240
- Lin, C. Y., Lin, C. C. H., Liu, J. Y., Rajesh, P. K., Matsuo, T., Chou, M. Y., et al. (2020). The early results and validation of FORMOSAT-7/COSMIC-2 space weather products: Global ionospheric specification and Ne-aided Abel electron density profile. *Journal of Geophysical Research: Space Physics*, 125(10), 1–12. https://doi.org/10.1029/2020JA028028
- Lin, C. Y., Matsuo, T., Liu, J. Y., Lin, C. H., Huba, J. D., Tsai, H. F., & Chen, C. Y. (2017). Data assimilation of ground-based GPS and radio occultation total electron content for global ionospheric specification. *Journal of Geophysical Research: Space Physics*, 122(10), 10–810. https://doi.org/10.1002/2017JA024185
- Lin, C. Y., Matsuo, T., Liu, J. Y., Lin, C. H., Tsai, H. F., & Araujo-Pradere, E. A. (2015). Ionospheric assimilation of radio occultation and ground-based GPS data using non-stationary background model error covariance. *Atmospheric Measurement Techniques*, 8(1), 171–182. https://doi.org/10.5194/amt-8-171-2015
- Liu, J. Y., Lin, C. Y., Lin, C. H., Tsai, H. F., Solomon, S. C., Sun, Y. Y., et al. (2010). Artificial plasma cave in the low-latitude ionosphere results from the radio occultation inversion of the FORMOSAT-3/COSMIC. *Journal of Geophysical Research*, 115(7), 1–8. https://doi.org/10.1029/2009JA015079
- Lugaz, N. (2020). PROSWIFT bill and the 2020 space weather operations and research infrastructure workshop from the national academies of sciences, engineering, and medicine. Space Weather, 18(10), e2020SW002628. https://doi.org/10.1029/2020SW002628
- Maruyama, N., Sun, Y.-Y., Richards, P. G., Middlecoff, J., Fang, T.-W., Fuller-Rowell, T. J., et al. (2016). A new source of the midlatitude ionospheric peak density structure revealed by a new ionosphere-plasmasphere model. *Geophysical Research Letters*, 43(6), 2429–2435. https://doi.org/10.1002/2015g1067312
- Masutani, M., Andersson, E., Terry, J., Reale, O., Jusem, J. C., Riishojgaard, L. P., et al. (2007). Progress in Joint OSSEs A new nature run and international collaboration. In Proceedings of the 12th conference on integrated observing and assimilation systems for atmospheres, oceans, and land surface (Ioas-Aols).
- Matsuo, T., & Hsu, C.-T. (2021). Inference of hidden states by coupled thermosphere-ionosphere data assimilation: Applications to observability and predictability of neutral mass density. *Upper Atmosphere Dynamics and Energetics*, 343–363. https://doi.org/10.1002/9781119815631.
- Matsuo, T., Lee, I. T., & Anderson, J. L. (2013). Thermospheric mass density specification using an ensemble Kalman filter. *Journal of Geophysical Research: Space Physics*, 118(3), 1339–1350. https://doi.org/10.1002/jgra.50162
- Moreno, B., Radicella, S., De Lacy, M. C., Herraiz, M., & Rodriguez-Caderot, G. (2011). On the effects of the ionospheric disturbances on precise point positioning at equatorial latitudes. GPS Solutions, 15(4), 381–390. https://doi.org/10.1007/s10291-010-0197-1
- Pedatella, N. M., Anderson, J. L., Chen, C. H., Raeder, K., Liu, J., Liu, H. L., & Lin, C. H. (2020). Assimilation of ionosphere observations in the whole atmosphere community climate model with thermosphere-ionosphere extension (WACCMX). *Journal of Geophysical Research: Space Physics*, 125(9), 1–15. https://doi.org/10.1029/2020JA028251
- Pedatella, N. M., Yue, X., & Schreiner, W. S. (2015). An improved inversion for FORMOSAT-3/COSMIC. *Journal of Geophysical Research:* Space Physics, 120(10), 8942–8953. https://doi.org/10.1002/2015JA021704
- Qian, L., Burns, A. G., Emery, B. A., Foster, B., Lu, G., Maute, A., et al. (2014). The NCAR TIE-GCM: A community model of the coupled thermosphere/ionosphere system. *Modeling the ionosphere-thermosphere system*, 201, 73–83. https://doi.org/10.1029/2012GM001297
- Richmond, A. D., Ridley, E. C., & Roble, R. G. (1992). A thermosphere/ionosphere general circulation model with coupled electrodynamics. Geophysical Research Letters, 19(6), 601–604. https://doi.org/10.1029/92GL00401
- Scherliess, L., Schunk, R. W., Sojka, J. J., & Thompson, D. C. (2004). Development of a physics-based reduced state Kalman filter for the ionosphere. *Radio Science*, 39(1), 231–242. https://doi.org/10.1029/2002rs002797
- Schreiner, W. S., Sokolovskiy, S. V., Rocken, C., & Hunt, D. C. (1999). Analysis and validation of GPS/MET radio occultation data in the ionosphere. *Radio Science*, 34(4), 949–966. https://doi.org/10.1029/1999rs900034
- Tsai, L. C., Liu, J. Y., Schreiner, W. S., & Berkey, F. T. (2001). Comparisons of GPS/MET retrieved ionospheric electron density and ground based ionosonde data. *Earth Planets and Space*, 53(3), 193–205. https://doi.org/10.1186/BF03352376
- Tsai, L. C., & Tsai, W. H. (2004). Improvement of GPS/MET ionospheric profiling and validation using the Chung-Li ionosonde measurements and the IRI model. *Terrestrial, Atmospheric and Oceanic Sciences*, 15(4), 589–607. https://doi.org/10.3319/TAO.2004.15.4.589(A
- Tulasi Ram, S., Su, S. Y., Tsai, L. C., & Liu, C. H. (2016). A self-contained GIM-aided Abel retrieval method to improve GNSS-Radio occultation retrieved electron density profiles. GPS Solutions, 20(4), 825–836. https://doi.org/10.1007/s10291-015-0491-z
- Vourlidas, A., Turner, D., Biesecker, D., Coster, A., Engell, A., Ho, G., et al. (2023). The NASA space weather science and observation gap analysis. Advances in Space Research. https://doi.org/10.1016/j.asr.2023.06.046
- Wu, D. L. (2018). New global electron density observations from GPS-RO in the D- and E-Region ionosphere. Journal of Atmospheric and Solar-Terrestrial Physics, 171, 36–59. https://doi.org/10.1016/j.jastp.2017.07.013
- Yue, X., Schreiner, W. S., & Kuo, Y.-H. (2013). Evaluating the effect of the global ionospheric map on aiding retrieval of radio occultation electron density profiles. GPS Solutions, 17(3), 327–335. https://doi.org/10.1007/s10291-012-0281-9
- Yue, X., Schreiner, W. S., Kuo, Y. H., Braun, J. J., Lin, Y. C., & Wan, W. (2014). Observing system simulation experiment study on imaging the ionosphere by assimilating observations from ground GNSS, LEO-based radio occultation and ocean reflection, and cross link. *IEEE Transactions on Geoscience and Remote Sensing*, 52(7), 3759–3773. https://doi.org/10.1109/TGRS.2013.2275753
- Yue, X., Schreiner, W. S., Lei, J., Sokolovskiy, S. V., Rocken, C., Hunt, D. C., & Kuo, Y. H. (2010). Error analysis of Abel retrieved electron density profiles from radio occultation measurements. *Annales Geophysicae*, 28(1), 217–222. https://doi.org/10.5194/angeo-28-217-2010

DIETRICH ET AL. 19 of 20



10.1029/2024SW003958

Yue, X., Schreiner, W. S., Pedatella, N., Anthes, R. A., Mannucci, A. J., Straus, P. R., & Liu, J. Y. (2014). Space weather observations by GNSS radio occultation: From FORMOSAT-3/COSMIC to FORMOSAT-7/COSMIC-2. Space Weather, 12(11), 616–621. https://doi.org/10.1002/2014SW001133

Zhang, S., Wu, X., & Hu, X. (2023). Ionospheric vertical correlation distance calculation based on COSMIC electron density profile data. *Journal of Geophysical Research: Space Physics*, 128(7), e2023JA031453. https://doi.org/10.1029/2023JA031453

DIETRICH ET AL. 20 of 20